Diamond formation by carbon saturation in C-O-H fluids during cold subduction of oceanic lithosphere

Maria-Luce Frezzotti[1], Jan-Marten Huizenga[2,3], Roberto Compagnoni[4], Jane Selverstone[5]

(1) Department of Earth and Environmental Sciences, University of Milano Bicocca, Piazza della Scienza 4, 20124 Milano, Italy. e-mail: maria.frezzotti@unimib.it

(2) Unit for Environmental Sciences and Management, North-West University, Potchefstroom, South Africa. e-mail: jan.huizenga@nwu.ac.za

(3) Economic Geology Research Unit (EGRU), School of Earth and Environmental Sciences, James Cook University, Townsville 4811, Australia. e-mail: jan.huizenga@jcu.edu.au

(4) Earth Science Department, the University of Torino, Via Valperga Caluso 35, Torino 10125, Italy. e-mail: roberto.compagnoni@unito.it

(5) Department of Earth and Planetary Sciences, University of New Mexico, Albuquerque, NM 87131-0001, USA. e-mail: selver@unm.edu

ABSTRACT

Microdiamonds in garnet of graphite-free ultrahigh pressure metamorphic (UHPM) rocks from Lago di Cignana (western Alps, Italy) represent the first occurrence of diamond in a low-temperature subduction complex of oceanic origin (T = ~600°C; $P \geq 3.2$ GPa). The presence of diamonds in fluid inclusions provides evidence for carbon transport and precipitation in an oxidized H_2O-rich C-O-H crustal fluid buffered by mineral equilibria at sub-arc mantle depths. The structural state of carbon in fluid-precipitated diamonds was analyzed with 514 nm excitation source confocal Raman microspectroscopy. The first order peak of sp^3-bonded carbon in crystalline diamonds lies at 1331 (± 2) cm^{-1}, similar to diamonds in other UHPM terranes. The analysis of the spectra shows additional Raman features due to sp^2 carbon phases indicating the presence of both hydrogenated

carbon (assigned to trans-polyacetylene segments) in grain boundaries, and graphite-like amorphous carbon in the bulk, i.e. showing a structural disorder much greater than that found in graphite of other UHPM rocks. In one rock sample, disordered microdiamonds are recognized inside fluid inclusions by the presence of a weaker and broader Raman band downshifted from 1332 to 1328 cm^{-1}. The association of sp^3- with sp^2-bonded carbon indicates variable kinetics during diamond precipitation. We suggest that precipitation of disordered sp^2 carbon acted as a precursor for diamond formation outside the thermodynamic stability field of crystalline graphite. Diamond formation started when the H_2O-rich fluid reached the excess concentration of C required for the spontaneous nucleation of diamond. The interplay of rock buffered f_{O_2} and the prograde *P*-*T* path at high pressures controlled carbon saturation. Thermodynamic modeling confirms that the C-O-H fluids from which diamond precipitated must have been water rich ($0.992 < X_{H2O} < 0.997$), assuming that f_{O_2} is fixed by the EMOD equilibrium.

KEYWORDS: diamond, C-O-H fluid, ultrahigh pressure metamorphism, Western Alps, Raman spectroscopy.

1. INTRODUCTION

The origin of microdiamonds in ultrahigh pressure metamorphic (UHPM) terranes recrystallized at subduction-zone depths of ≥100 km is a significant geological question, because it affects Earth's cycling of crustal carbon. The most widely accepted hypothesis concerning the origin of metamorphic diamonds is crystallization from mobile C-bearing phases (C-O-H fluids/melts) (Shatsky et al., 1995, 2000; de Corte et al., 1998; Ogasawara et al., 2000; Cartigny et al., 2001; Dobrzhinetskaya et al., 2001, 2003a,b; Hwang et al., 2001, 2003; Stöckhert et al., 2001; Massonne, 2003; Ogasawara, 2005; Korsakov and Hermann, 2006; Sitnikova and Shatsky, 2009; Dobrzhinetskaya, 2012), although solid-state transformation from graphite in absence of fluid/melt phases has also been proposed (; (Korsakov et al., 2010).

Metamorphic diamonds generally occur in continental-collision terranes of Paleozoic – Mesozoic age (cf., Carswell and Compagnoni, 2005). At present, confirmed UHPM terranes (Dobrzhinetskaya, 2012) include: the Kokchetav massif, Kazakhstan (Sobolev and Shatsky, 1990; Dobrzhinetskaya et al., 1994, 2003a; De Corte et al., 2000; Korsakov et al., 2002, 2010; Smith et al., 2011); the Western Gneiss Region, Norway (Dobrzhinetskaya et al., 1995; van Roermund et al., 2002; Vrijmoed et al., 2006; 2008; Janák et al., 2013; Smith and Godard, 2013); the Dabie and Qin Lin regions, China (Xu et al., 1992; Yang et al., 2003; Li et al., 2013), the Saxonian Erzgebirge other places within the Moldanubian zone of the Bohemian massif, Germany (Massonne, 1999; Stöckhert et al., 2001; Naemura et al., 2011; Kotková et al., 2011), Rhodope massif, Greece (Mposkos and Kostopoulos, 2001; Perraki et al., 2006; Schmidt et al., 2010).

Recently, microdiamonds have been described in UHP ocean floor metasediments at Lago di Cignana Unit (LCU) in the western Alps, Italy (Frezzotti et al., 2011). This new diamond discovery has several characteristics which are well suited to study carbon transport and for controlling redox gradients during deep subduction: i) host metamorphic rocks are of oceanic rather than continental affinity ii) diamond formation occurred at low temperatures (≤600°C) and at pressures consistent

with subarc depths (≥ 3.2GPa; Groppo et al., 2009), and iii) diamond precipitated from an oxidized, carbonate-bearing H_2O-rich fluid buffered by mineral equilibria (Frezzotti et al., 2011).

Although nucleation and growth of metamorphic diamonds at low temperatures has long been proposed (e.g., 300 to 500 °C, Griffin et al., 2000; 500 to 700 °C, Cartigny et al., 2001; 600° C, Bostick et al., 2003), it has rarely been taken in account for modeling carbon behavior during deep subduction. Diamond crystallization in oxidized, C-O-H fluids or melts reacting with minerals has been studied experimentally and in other UHP terranes at considerably higher temperature and pressure conditions (P > 4-5 GPa; T > 900°C) than those of the LCU unit (Sobolev and Shatsky, 1990; Pal'yanov et al., 1998; Sato et al., 1999; Sokol et al., 2000, 2001, 2004; Arima et al., 2002; Sokol and Pal'yanov, 2004; Spivak and Litvin, 2004; Ogasawara, 2005; Korsakov et al., 2010; Dobrzhinetskaya, 2012; Schertl and Sobolev, 2012). At these higher P-T conditions, the distinction between aqueous fluid phases and silicate melts is not possible because volatile-rich chemical systems are in a supercritical state, or very close to it (Bureau and Keppler, 1999; Akaishi and Yamaoka, 2000; Pal'yanov et al., 2002; Manning, 2004; Ferrando et al., 2005; Frezzotti et al., 2007). In addition, existing models generally do not consider the relative interplay of the driving forces (pressure, temperature, oxygen fugacity) that are applicable to fluid speciation and diamond-forming reactions, and clearly do not fully capture the properties and behavior of carbon during active subduction. In dynamic systems, such as a subducting oceanic lithosphere, the interplay between changing temperature, pressure, and oxygen fugacity by fluid-rock interactions can cause large differences in carbon transport by C-O-H fluids and results in redox gradients.

In order to investigate the formation of metamorphic diamond from C-bearing oxidized fluids, we performed a detailed micro-Raman spectroscopic study of carbon allotropes in garnetites from LCU. Among conventional techniques suitable for the study of carbon, Raman microspectroscopy has already proven to be by far the most powerful. Not only does it provides basic crystalline phase identification (e.g., carbon allotropes), but subtle spectra modifications can be used to characterize micro- to nano-scale structural states. We show how the kinetics of C-

95 saturation in carbonate-bearing H_2O-rich fluids, in conjunction with parameters such as temperature
96 and pressure, could influence the structural state of fluid-precipitated carbon and consequent
97 diamond nucleation and growth. We also propose a thermodynamic model to explain the complex
98 *P–T–* f_{O_2} dependent fluid-rock interaction during subduction, inducing diamond nucleation,
99 growth, and eventual dissolution in crustal fluids.
100

101 ## *2. METAMORPHIC EVOLUTION OF DIAMOND-BEARING UHP UNIT OF LAGO DI*
102 ## *CIGNANA (W ALPS)*

103 The ultrahigh-pressure (UHP) Lago di Cignana Unit (LCU) is exposed in the upper
104 Valtournenche, Aosta valley, Italian western Alps (Fig. 1). It is part of the Piemonte Zone of calc-
105 schists with meta-ophiolites, derived from the ocean basin that separated the European continent to
106 the NW from the Apulia (or Adria) plate to the SE in late Jurassic time (Dal Piaz, 1974; Dewey et
107 al., 1989; Polino et al., 1990; Lombardo et al., 2002 and references therein). In the upper
108 Valtournenche, the Piemonte Zone consists of a pile of tectonic slivers including epidote–blueschist
109 to lawsonite–blueschist facies (Combin Zone) and eclogite facies (Zermatt–Saas Zone) Alpine
110 metamorphic rocks as defined by Bearth (1967). These two main ensembles of tectonic units of
111 meta-ophiolites and metasediments are sandwiched between two continental units, the overlying
112 Austroalpine Dent Blanche and the underlying Penninic Monte Rosa massif (Fig. 1).
113 The LCU is best exposed on the southern side of the artificial lake of Cignana (Fig. 1b). The
114 unit consists of 3 main slivers c. 1000, 350 and 250 m long, respectively, and is less that about 100
115 m thick (Forster et al., 2004; Fig. 1). It is overlain by a thin skin of highly deformed metagabbro
116 from the Zermatt-Saas Zone that separates it from the overlying garnet-bearing metabasics
117 considered part of the Combin Zone by Forster et al. (2004), but belonging to the Zermatt-Saas zone
118 according to Pleuger et al. (2007) and Groppo et al. (2009) on the basis of petrological and
119 structural data. The lower contact of the LCU is with a thick sequence of layered metagabbro and

antigorite serpentinite of the Zermatt-Saas Zone (Forster et al., 2004). Thus, the LCU is enclosed and enveloped by sheared tectonic slices derived from the Zermatt-Saas Zone.

The UHP unit consists of a basement of glaucophane eclogites with zoisite/clinozoisite + paragonite pseudomorphs after lawsonite, derived from original basalts, and a metasedimentary cover series, which includes micaschists, impure marbles and quartzites with nodules or boudinaged layers of Mn-rich garnetites with black Fe-Mn nodules (Bearth, 1967; Dal Piaz et al., 1979). The diamonds occur in the Mn-rich garnetites that likely reflect Mn nodules and crusts. The manganiferous quartzites (Bearth, 1967; Dal Piaz et al., 1979) became well known among the UHPM community after the discovery by Reinecke (1991, 1998) of coesite included in a tourmaline crystal. Peak metamorphic conditions were estimated at 615 ± 15 °C and 2.8 ± 1.0 GPa by Reinecke (1991, 1998) from metasediments and Reinecke et al. (1994) from basaltic eclogites. The exhumation history of the unit has been reconstructed on the basis of microstructural analysis of metabasics by van der Klauw et al. (1997). King et al. (2004) showed that garnet from eclogites preserves trace element evidence of prograde discontinuous reactions.

Recently, Angiboust et al. (2009), in a comprehensive study of the Zermatt-Saas unit eclogites and metasediments exposed to the north of the Gran Paradiso massif, obtained peak metamorphic conditions around 540 ± 20 °C and 2.3 ± 0.1 GPa. In this picture, the higher *P*-*T* conditions shown by the Lago di Cignana lithologies are interpreted as possibly due to: (1) the detachment of hectometer-scale portions deeper than the rest of the ophiolite and later juxtaposed at 2.3–2.5 GPa, or (2) small overpressures within the Lago di Cignana eclogitic unit, as predicted in the subduction channel from numerical experiments (ca. 10%: Yamato et al., 2007; Raimbourg and Kimura, 2008). Recently, Groppo et al. (2009), studying in detail the metamorphic evolution of the meta-ophiolites of LCU and of the adjoining units, concluded that the peak assemblage garnet + omphacite + Na-amphibole + lawsonite + coesite + rutile formed at $T = \sim 600$°C and $P \geq 3.2$ GPa, i.e. in the diamond stability field (Day, 2012). These unusually high-pressure conditions were

145 further supported by Frezzotti et al. (2011), who discovered microdiamond inclusions in
146 spessartine-rich garnets from the LCU quartzitic sedimentary cover.
147
148 *3. PETROGRAPHY OF THE IMPURE QUARTZITE AND THE MANGANIFEROUS*
149 *GARNETITE*
150 The impure quartzites including manganiferous garnetites consist, in addition to quartz and
151 garnet (> 80% in vol.), of minor phengite, partly chloritized green-brownish biotite, piemontite, a
152 possibly pre-tectonic epidote, with a light purple radioactive core, arranged perpendicular to the
153 main foliation, and accessory rutile, opaque ores (most likely Mn-oxides), apatite and a slightly
154 zoned pale green tourmaline. More than one generation of white micas may be recognized on the
155 basis of the microstructural site, grain size and interference colors. The pale pink manganoan
156 phengite (Reinecke, 1991) crystallized with the uniaxial 3T polytype. The arrangement of phengite
157 flakes and the local presence of isoclinals fold hinges indicate that the main foliation is a
158 transposition foliation.
159 The original manganiferous garnetite occurs in the quartzite as a few cm-thick discontinuous
160 pink to red-brown layers, knots or nodules that in some cases appear to have formed by boudinage
161 of original layers. Some nodules appear to be hinges of rootless isoclinal folds. Garnetite consists of
162 an inner portion of massive, close packed, equigranular aggregate of small (c. 50-300 μm across)
163 welded garnets and accessory rutile and apatite. Thin films of quartz between garnet granoblasts
164 occur locally. The original, almost monomineralic garnetite is usually dismembered into fragments
165 with angular shapes separated and cemented by a network of fractures healed with quartz (Fig. 2a).
166 Locally, this quartz is recrystallized to poikiloblasts up to 2 cm across, with a subgrain
167 microstructure whose grain size is similar to that of the surrounding quartzite. Moving further away
168 from the garnetite core, the quartz-garnet ratio increases, but the shape of the nodule is usually still
169 preserved. In this portion, garnets, which are unevenly arranged, may have coarser grain-size and

atoll-like shape with a colorless, euhedral, inclusion-free corona surrounding a corroded pink core that is crowded with inclusions.

In the massive garnetite, where garnets show a granoblastic microstructure and are welded together, individual garnet crystals can be recognized by the presence of reddish, inclusion-rich cores surrounded by colorless rims (Fig. 2). Inclusions comprise opaque phases, quartz/coesite, magnesite, dolomite, and carbonates (Fig. 2b). Mineral inclusions have sizes from 10 to 200 μm and show rounded or elongated shapes. Coesite and quartz are commonly present as single crystals, and the usual petrographic features associated with the coesite-quartz transition are lacking (i.e. visible coesite relic; palisade-textured quartz; polycrystalline quartz mosaic).

Garnets also contain rare microdiamond inclusions (Fig. 2b), ranging from 1 to 20 μm in size, with an average size of 2-6 μm. They are blackish, subhedral to euhedral, and often show well-developed cuboidal and octahedral morphologies (Fig 2b and 3). Their distribution is limited to garnet cores where they generally occur as groups of 2 or more, always associated with carbonate and aqueous fluid inclusions (i.e., coeval; Fig. 3a, b, and c). Graphite has not been observed. Water-rich fluid inclusions (2-30 μm in size) also contain microdiamonds, along with several daughter crystals (Fig. 3a and d), including Mg-calcite/calcite, quartz, rutile, paragonite, ± dawsonite, ± rhodochrosite, ± hydrous Mg-carbonates and sulfates (e.g., dypingite $Mg_5(CO_3)_4(OH)_2 \cdot 5H_2O$, and pentahydrite $MgSO_4 \cdot 5H_2O$). Previous Raman studies detected bicarbonate, sulfate, carbonate ions, and H_4SiO_4 monomers and dimers in the aqueous fluid, while no CO_2 ($X_{CO2} < 0.026$ at room temperature) (Frezzotti et al., 2011).

4. RAMAN MICROSPECTROSCOPY

We investigated phase purity and crystallinity of LCU microdiamonds by Raman micro-spectroscopy. This is one of the few techniques sensitive to the full range of structural states of carbon, and has been successful in studies of diamond, graphite, fullerenes, and other metastable

195 carbon allotropes. Distinctive Raman bands are observed for each of these individual forms of
196 carbon, making it possible to distinguish among sp^2 and sp^3 hybridization. The first-order band of
197 crystalline diamond occurs at 1332 cm^{-1} and is generated by vibrations of the two interpenetrating
198 cubic sublattices. The crystalline graphite band, referred to as "G band" (Ferrari and Robertson,
199 2000), lies at 1580 cm^{-1}, and results from vibrations in the graphene planes. In graphite, two
200 additional "D bands" (D = disorder) appear at 1350-1370 cm^{-1} (D_1) and 1620 cm^{-1} (D_2, as shoulder
201 to the G band) if grain size is reduced or graphene planes are curved (cf., Lespade et al., 1982; Roy
202 et al., 2003, and references therein). The D_1 band has peculiar features, such as the excitation
203 dependence of its wavenumber and the proximity to the diamond band, which have not yet been
204 fully explained (Ferrari and Robertson, 2000).
205 Diamonds were confirmed in four samples of garnetites. Eight doubly polished sections of
206 about 100 microns in thickness were made using Al_2O_3 as grinding and polishing medium. Polished
207 sections were analyzed without any other further treatment (e.g., gluing to glass) and analyzed on
208 both sides. The Raman spectra were collected in the 100-4000 cm^{-1} range using a Horiba (Jobin
209 Yvon) micro-Raman spectrometer (Labram) at the University in Siena. It comprises an integral
210 Olympus BX40 microscope with a 100× objective (n.a. = 0.9), which enhances confocality and
211 reduces the laser spot in the sample to 1×1×5 μm^3. The slit and pinhole were set at 100 µm in
212 confocal configuration to increase the laser spatial resolution. A holographic grating (1800
213 lines/mm) provides a spectral resolution of 1.5 cm^{-1}. All spectra were excited with visible Ar^+ laser
214 light (514.5 nm) with a power of 100-300 mW at the source (correspondingly, 80% lower at the
215 sample surface), and collected in the backscattering configuration. Collection time varied from 1 to
216 10 s with 1-5 times accumulations for each spectrum. Daily calibration was done referring to the
217 1332 (± 0.5) cm^{-1} first order band of diamond. The spectral reproducibility was better than ± 0.2
218 cm^{-1}. Spectra are reported with no baseline correction. A special precaution was taken to avoid
219 local heating of diamonds by the excitation laser (cf. Kagi et al., 1994). To achieve this, all

measurements of diamonds were carried out at low collection times and low excitation power. Mineral identification was based on our database of spectra (Frezzotti et al., 2012a).

Raman mapping of diamond and other inclusions in garnet was performed using a computer-controlled, automated X-Y mapping stage (HORIBA Jobin Yvon) with the capability of one moving step for 2 μm. The mapping area of 400 μm × 450 μm was focused on garnet 20 μm below the sample surface.

4.1 Diamonds

For diamonds included in garnet, the first order Raman band lies at 1332 (± 2) cm^{-1}, which is the revealing feature of its cubic structure (i.e., C-C bonding of sp^3-bonded C), shown in Fig. 4. More than 40 Raman bands of successfully identified diamonds have a band spread (FWHM; full width at half peak maximum intensity) of 3.5 - 7.6 cm^{-1}. Several spectra show the presence of an additional band around 1080-1088 cm^{-1} (Fig 4 b and c). The position of this band is compatible with the symmetric stretching vibration (ν_1) of the carbonate group in calcite. Based on a single Raman band, however, an unequivocal assignment is not possible. The FHWM of the carbonate band is extremely variable, suggesting a relevant disorder. Poorly crystalline carbonates were previously observed in kimberlitic diamonds (Kopylova et al., 2010; and references therein).

In fluid inclusions, the sharp diamond band lies at 1331 (± 3) cm^{-1} with FWHM values of 2.5 to 10 cm^{-1}, in agreement with the Raman spectra of diamond inclusions in garnet (Fig. 5). Some diamond bands have distinctly low intensity (compare Figs. 5a and b), suggesting that grain sizes are on the order (or smaller) of the Raman excitation spot diameter of 1μm. In fluid inclusions, diamonds coexist with several other daughter phases, such as carbonates, silica, rutile, ± sulfates (Fig. 5). Among carbonates, Na-Ca- anhydrous, hydrous, and hydrated carbonates dominate. A detailed list of daughter mineral spectra collected in fluid inclusions can be found in Frezzotti et al. (2011).

4.2 *Sp^2-bonded carbon in diamonds*

In many diamond Raman spectra, supplementary bands appear in the 1200 – 1600 cm^{-1} carbon region, which for the most part reflect sp^2 hybridization in carbon, either in the bulk crystal or on the grain surface. Band positions and assignments are shown in Table 1, and discussed below.

4.2.1 Graphite-like amorphous carbon

Two additional symmetric bands centered between ca. 1350-1370 (D1-band) and 1590-1605 cm^{-1} (G-band) in diamond spectra are characteristic for sp^2-bonded (i.e., virtually free of sp^3 bonding) carbon in graphite (Figs. 4, 5, and 6). The D1 band lies at that of graphite while the G band position is shifted from 1580 to about 1590-1605 cm^{-1} (Figs. 6a, b, and c) and matches those of carbon rings in threefold coordination with very low degree of crystal order, where no extended graphitic structure exists (Ferrari and Robertson, 2000). Tuinstra and Koenig (1970) found that the intensity of the D1-band (I_{D1}/I_G) is inversely proportional to the effective graphite crystallite size (Lg) in the direction of the basal plane, by the following empirical law:

$$\frac{I_{D1}^{1350\ cm-1}}{I_G^{1580\ cm-1}} = \frac{C\lambda\ (\mathrm{nm})}{Lg\ (nm)} \quad (1)$$

where C (λ = 514 nm) is 4.4 nm. A similar intensity of the D1 band to that of the G band (i.e., I_{D1}/I_G ratio > 1), like in Figs. 4b and 5b, is observed when the sizes of sp^2 clusters do not exceed tens of nanometers.

The intensity of the D_1 and G bands varies with the intensity of the diamond band, showing an apparent anticorrelation (Figs. 4 and 6). Moreover, the luminescence background intensity increases linearly with the increase of the D_1 and G bands (Fig. 6c).

Previous studies have attributed the D_1 band to various forms of non-diamond carbon phases: graphite-like amorphous carbon, disordered graphite, disordered glassy carbon, sp^2-hybridized carbon phases, microcrystalline defective graphite, inclusions of amorphous diamond-like carbon, or a diamond precursor phase (Ferrari and Robertson, 2000; Zaitsev, 2001). The graphite-like amorphous carbon portion inside diamond represents a subordinate, although variable, feature by volume generally not exceeding a few unit %. The Raman scattering coefficient for the sp^2 phase is about 50 times stronger than that for sp^3 phase, when using the laser 514 nm light as excitation source (Wada and Solin, 1981).

4.2.2 Hydrogenated carbon (CH)x-

Four diamond spectra show a band at about 1150 cm^{-1}, accompanied by another one at approximately 1450 cm^{-1}, as shown in Figs. 6a and b. These new Raman bands only appear in diamonds contained inside fluid inclusions. The attribution of these two bands is controversial. Some authors associated the presence of these two Raman bands to nanocrystalline diamond, a disordered precursor structure of diamond (Mitura, 2007; Mitura et al., 2006 and references therein). But Ferrari and Robertson (2001) and Birrell at al. (2005) argued that these bands should not be assigned to any sp^3-bonded phase, and instead suggested that these bands represent (CH)x (trans-polyacetilene) chains in sp^2-bonded configuration at the diamond surface. In our case, it is very unlikely that the 1150 and 1450 cm^{-1} bands arise from the presence of a disordered sp^3-hybridized carbon structure, since the degree of crystallinity of microdiamonds is very high as derived from their first-order band intensity and FWHM (Fig. 6a and b). Therefore, we attribute these spectral features to traces of carbon hydrogenation in grain boundaries, as proposed by Ferrari and Robertson (2001). Since carbon hydrogenation is observed only in diamonds contained within fluid inclusions, these data may suggest incipient diamond dissolution in aqueous fluids.

295 *4.3 Disordered diamonds*

296 Very unusual Raman spectra were collected in a few fluid inclusions in one sample (AlC2),
297 in which no microdiamond inclusions were detected in garnet. These spectra are characterized by
298 high luminescence background, and by the presence of several weak bands in the 1200-1600 cm^{-1}
299 carbon region (Fig. 6d). The most notable feature is a low-intensity band near 1332 cm^{-1}, which
300 indicates the existence of diamond grains. The diamond band, however, shows a significant
301 decrease in intensity and an increase in FWHM compared to crystalline diamonds. The band is also
302 shifted from 1332 cm^{-1}, which is the normal value for diamond, to 1327-1328 cm^{-1}.

303 In the first-order diamond band, the observed variation of intensity, position, and FWHM
304 can be indicative of distinct processes, such as: (1) local heating by a laser; (2) metamictization by
305 radioactive minerals; (3) nanometer-range size of individual crystallites; and (4) disorder in sp^3
306 bonded carbon (cf., Kagi et al., 1994; Orwa et al., 2000; Nasdala et al., 2004; Petrovsky et al., 2010;
307 Smith and Godard, 2009; Smith et al., 2011, and references therein).

308 Overheating by laser light does not represent a relevant mechanism: all Raman spectra were
309 acquired with the same analytical conditions, and the downshift + peak broadening was exclusively
310 observed in diamonds present in this sample. Metamictization of diamonds by radioactive minerals
311 can be excluded. Metamictic diamonds show additional distinctive Raman bands, which are absent
312 in our spectra (cf., Smith et al., 2011). Presence of nano-sized diamonds is also very unlikely since
313 it would require a grain size below 10 nm to record disorder at the surface (i.e., dangling bonds;
314 Watanabe et al., 2006). Therefore, observed Raman spectral features can be better explained by the
315 presence of many types of point and extended defects, lowering the crystallinity in diamond (cf.,
316 Smith and Godard, 2009). Since defects in minerals commonly induce fluorescence, structural
317 disorder in diamond would be in agreement with the high fluorescence background observed in
318 Raman spectra (Fig. 6d). Of particular interest are the two additional bands of similar intensity at
319 about 1285 and 1305 cm^{-1} (Fig. 6d; Table 1), which form a triplet with the defective diamond band.

These two bands are compatible with assignments reported for other diamond polytypes, such as hexagonal (2nH) lonsdaleite (Table 1; Le Guillou et al., 2007; Wu and Xu, 1998; Wu, 2007; Smith et al., 2011).

A relevant contribution of graphite to these spectra is indicated by the presence of the G and D1 bands, at 1564-1570 cm^{-1} and 1330-1380 cm^{-1}, respectively (Fig. 6d). The I_{D1}/I_G ratio corresponds to a much higher degree of crystallinity than previously described for sp^2-bonded carbon phases (cf., section 4.2), and provides evidence for the presence of metamorphic graphite in diamond (Wopenka and Pasteris, 1993; Beyssac et al., 2003; Frezzotti et al., 1994; Luque et al., 2009). The position of the G band tends to be displaced towards lower wavelengths (between 1575 and 1585 cm^{-1}), which could highlight additional local structural parameters (e.g., presence of cracks, stress, etc.).

4.4 Raman maps of garnet containing diamonds

The host spessartine (Fig. 7a) shows main bands at 171, 202, 221, 327, 353, 375, 474, 506, 556, 631, 848, 876, 906, and 1029 (± 2) cm^{-1}, which represent the A_{1g}, E_g and T_{1g} Raman modes active in this cubic garnet. None of these bands interfere with sp^2- and sp^3-hybridized carbon vibrations, which lie at higher wavelengths. In the Raman spectra of spessartine core regions, a strong intensity hardening of all internal (SiO_4) and external (lattice) A_{1g} modes is observed adjacent to diamond, quartz, magnesite, and fluid inclusions (A-type symmetry in garnet; blue spectrum in Fig. 7c), though analyses were performed without any variation either in orientation or in the analytical conditions. This effect is absent in garnet areas adjacent to coesite.

We used this property to generate a spectroscopic image of a garnet core containing diamonds and other inclusions (Fig. 7a). Fig. 7b maps the increased Raman intensity ratio for the (Si-O) symmetric stretching mode (A_{1g}) at 906 cm^{-1} with respect to the (Si-O) asymmetric stretching mode (T_{1g}) of SiO_4 units at 848 cm^{-1} in garnet (I_{906} / I_{848}; Fig. 7c). The distribution of the increase of the

346 A_{1g} mode intensity and of the concomitant decrease of the T_{1g} mode intensity in areas adjacent to
347 inclusions can be easily observed with the different colors of the map (from black to yellow; see
348 also the two spectra in Fig. 6c). Since A_{1g} modes in garnet originate from the movements of O
349 relative to Si in tetrahedra, they are not dependent on the nature of the cations. Hardening of A_{1g}
350 mode intensity in spectra could not have been induced by a variation in garnet composition (e.g.,
351 increase of almandine, pyrope, or calderite component), which results in a variable shifting of the
352 main Raman bands in the complex garnet structure (Bersani et al., 2009).
353 A reduction of the symmetry patterns (e.g., distortion of octahedral Mn^{3+}) can make the cubic
354 garnet appear to have A-type symmetry (Hatch and Griffin, 1989; Hofmeister et al., 2004).
355 Reduction of symmetry could indicate high strain in these regions, induced by very local
356 overpressures between inclusions formed at high pressure and surrounding garnet, due to a thermal-
357 expansion mismatch during exhumation at low temperatures. Alternatively, it could suggest the
358 local presence of tetragonal Mn-hydrogarnet (e.g., henritermierite; $Ca_3Mn^{3+}{}_2[SiO_4]_2[OH]_4$;
359 Kobayashi and Shoji, 1987; Armbruster and Lager, 1989; Lager et al., 1989; Armbruster, 1995).
360 The latter hypothesis, however, seems unlikely since OH^- bands were not observed in garnet Raman
361 spectra.
362

363 ## *5. DISCUSSION*

364 ### *5.1 Diamond nucleation and crystallization in C-O-H fluids*

365

366 The LCU diamonds display most of the typical features of metamorphic microdiamonds in
367 UHPM terranes (cf., de Corte et al., 1998; Perraki et al., 2006; Dobrzhinetskaya et al., 2005; 2007;
368 Dobrzhinetskaya, 2012; and references therein), including: i) cuboidal and octahedral
369 morphologies, ii) dimensions up to a few tens of micrometers, iii) generally high crystallinity (main
370 Raman band position and FHWH), iv) presence as inclusions in both minerals and fluid inclusions,

371 and v) independent petrological *P*-*T* estimates which constrain pressure conditions in the diamond
372 stability field.
373 Microdiamonds in UHPM rocks of LCU provide one line of evidence in favor of carbon
374 transport and precipitation by C-saturation in a C-O-H fluid phase buffered by mineral equilibria at
375 pressures ≥ 3.2 GPa (Frezzotti et al., 2011). The proof is the presence of diamonds contained in
376 fluid inclusions. Graphite conversion does not appear a relevant process in the formation of
377 diamonds, as indicated by the absence of metamorphic graphite in LCU garnetite samples. Also,
378 estimated peak metamorphic temperatures around 600°C ($P \geq 3.2$ GPa) are beyond doubt too low to
379 overstep the kinetic barrier necessary to break sp^2 bonds and to fix sp^3 C symmetry (cf., Bundy and
380 Kasper, 1967).
381 LCU diamonds allow us to model carbon behavior in crustal fluids during subduction to
382 depths of around 100 km. Since LCU diamonds were formed in rocks originating from oceanic
383 sediments rich in H_2O, carbonates and/or hydrocarbons, it is very likely that the carbon reservoir for
384 LCU diamonds is crustal. A link between the subducted protholith and diamond is suggested by the
385 common presence of carbonate inclusions (i.e., dolomite and magnesite) in spessartine, and the
386 nature of metamorphic fluid phases. Diamond forming fluids were oxidized, H_2O-rich, and in the
387 carbonate-C system, as indicated by the detection of HCO_3^- and CO_3^{2+} species in solution, and by
388 the absence of significant molecular CO_2 (≤ 2.6 mol.%).
389 The precipitation of diamond was induced by a redox interaction between iron-bearing
390 silicates in rocks (e.g., garnet) (Malaspina et al., 2009) and carbonates (in the fluid phase) at peak
391 metamorphic conditions ($P \geq 3.2$ GPa; $T = 600$°C), such as (Frezzotti et al., 2011):
392
393 $2CaFe(CO_3)_2$ (in dolomite) + $CaCO_3$ + $3SiO_2$ = $Ca_3Fe_2Si_3O_{12}$ + 5C + 9/2 O_2 (2)
394
395 The following Raman observations on the structural states of carbon can provide important
396 information on the kinetics of nucleation and crystallization of diamonds in C-O-H fluid:

1) Microdiamonds generally show high crystallinity in grains down to the micron size range.
2) Highly disordered graphitic units are detected in bulk diamond (sp^2 bond abundance ≤ 1-5 %). Raman bands correspond to a sp^2 carbon network of nano-sized in-plane graphite crystallites.
3) A continuous or discontinuous CH^- (trans-polyacetylene) layer is present at the surface of a few microdiamonds contained in aqueous fluid inclusions.
4) Disordered microdiamonds are present in fluid inclusions of one sample that lacks crystalline diamonds. Disorder in diamonds is probably associated with the presence of other sp^3-bonded carbon allotropes (e.g., lonsdaleite ?).

The Raman structural features showing graphite-like amorphous carbon associated with highly crystalline diamonds at LCU are unexpected. Sp^2-bonded carbon intergrown with diamonds is known in UHPM terranes, but it shows a much higher degree of order (i.e. much lower I_{D1}/I_G ratio in Raman spectra) corresponding to polycrystalline (i.e., metamorphic) graphite (Khokhryakov et al., 2009; Korsakov et al., 2010, and references therein). Spectral features of disordered sp^2 carbon detected by present study are not compatible with temperatures attained at peak metamorphism (i.e., 600°C), or during exhumation (cf., Wopenka and Pasteris, 1993; Beyssac et al., 2003), and exclude an origin by retrograde diamond graphitization.

The association at the micron scale of sp^3- with sp^2-bonded carbon in many diamonds provides evidence that some sort of variable kinetics induced the precipitation of a succession of distinct carbon allotropes, likely due to varying *P*-*T*- f_{O_2} conditions. We suggest that disordered sp^2-bonded carbon indicates the presence of a metastable phase acting as a precursor for diamond formation in H_2O rich-fluids outside the thermodynamic stability field of crystalline graphite. For sp^2-bonded carbon, it has been proposed that crystallization in a *P*-*T* regime where diamond is actually thermodynamically stable with respect to graphite should be expected at low temperatures due to sluggish kinetics (Pal'yanov et al., 2002b; Sokol et al., 2000, 2001; Okada et al., 2004;

Dobrzhinetskaya, 2012). In addition, Foustoukos (2012) reported the formation of similar (i.e. I_{D1}/I_G in Raman spectra) disordered graphitic carbon as precursor state - preceding the crystallization of the well-ordered phase - during hydrous experiments at 600°C.

This is probably because numerous sp^2-bonded carbon nuclei formed from the beginning and the nucleation barrier for diamond in C-saturated aqueous fluids was very high at low temperatures. Therefore, the dissolved carbon first crystallized as metastable sp^2 carbon. As the concentration of carbon atoms in the fluid gradually increased, diamond formation would have started when the fluid reached the excess concentration of C required for the spontaneous nucleation of diamond. As pointed out by Pal'yanov et al. (2007), a similar nucleation and crystallization history suggests a variation in the C-O-H fluid composition (i.e., enrichment in carbon). Since the fluid composition was buffered by redox reactions between the fluid and the host rock during subduction, it is conceivable that the interplay of f_{O_2} buffer and prograde *P-T* path provided gradient-driven C-saturation ($a_C^{fluid} = 1$) paths of fluids during diamond formation at high pressures.

Retrograde graphite conversion is not observed in crystalline diamonds. However, the presence of a polyacetylene shell in the surface of a few microdiamonds contained in fluid inclusions suggests incipient dissolution (cf., O'Bannon et al., 2012; Xia et al., 2013). Since this process affected only those diamonds that remained in the aqueous inclusions for the whole *P-T* path, dissolution indicates a gradient towards C undersaturation ($a_C^{fluid} < 1$) in C-O-H fluid during retrogression and exhumation of the host garnetites. For those diamonds contained in garnet, isolation most likely prevented retrograde interaction with aqueous fluids.

The formation of defective microdiamond grains with variable degrees of structural disorder requires a different mechanism of crystallization. These diamonds do not appear to have spontaneously nucleated during the prograde *P-T-* f_{O_2} path. Diamond is the stable phase at pressures greater than those of the thermodynamic stability field of crystalline graphite. However, its degree of structural order is also function of chemical or kinetic factors (e.g., temperature and degree of C-

447 saturation). Thus, it is likely that these thermodynamically less stable diamonds grew rapidly by C-
448 supersaturation, on fluid cooling in the diamond stability field. Their presence, limited to a few fluid
449 inclusions in one sample where crystalline diamonds are noticeably absent, suggests that disordered
450 diamond crystallization was induced by local processes, such as a relative C-enrichment of aqueous
451 fluids by water diffusion from single inclusions during early retrogression (cf., Frezzotti et al.,
452 2012b). Metamorphic graphite conversion is observed in these thermodynamically less stable
453 diamonds, which can be more easily graphitized than crystalline diamonds (cf., Smith et al., 2011).
454
455 *5.2 Thermodynamic modeling of P-T-* f_{O_2} *evolution from C-O-H fluid phases*
456
457 We have applied thermodynamic calculations in order to get a better understanding on *P*, *T*,
458 and f_{O_2} fluid evolution and diamond formation. The C-O-H fluid system is considered to comprise
459 H_2O, CO_2, CH_4, CO, H_2, and O_2 at the *P-T* conditions of interest. A C-O-H fluid is divariant at a
460 fixed pressure and temperature. This implies that if the oxygen fugacity (f_{O_2}) and an additional
461 compositional constraint are known, the fluid composition and a_C^{fluid} can be calculated. The a_C^{fluid} is
462 a critical fluid system parameter in this study: it determines whether diamond/graphite will be in
463 equilibrium with the fluid phase ($a_C^{fluid} = 1$) or may be dissolved by the fluid phase ($a_C^{fluid} < 1$).
464 Calculations were performed assuming redox equilibrium between the host-rock and the fluid
465 phase, i.e. $f_{O_2}^{fluid} = f_{O_2}^{rock}$ (referred to as $f_{O_2}^{fluid/rock}$ from here onwards). The Gibbs energy minimization
466 method by Zhang and Duan (2009, 2010) is used to perform C-O-H fluid calculations, using the
467 Excel spreadsheet GFluid (Zhang and Duan, 2010). The GFluid model reproduces experimental C-
468 O-H fluid speciation datasets accurately showing average deviations of 1.5% (Zhang and Duan,
469 2009). We modified this spreadsheet for our specific needs by including our own f_{O_2} buffer
470 reactions.

The *P-T* conditions of diamond precipitation are constrained by the prograde *P-T* path of the Lago di Cignana unit, which was derived from pseudosections using metabasite and eclogite rock samples (Groppo et al., 2009). The maximum *T* and *P* conditions of the Lago di Cignana unit is ~600°C and ≥ 3.2 GPa (Groppo et al., 2009), respectively. As the maximum *P* is not well constrained, we also considered a modified *P-T* path with a maximum *P* of ~4 GPa (Fig. 8). Depending on which diamond-graphite transition curve is selected (e.g., Kennedy and Kennedy, 1976; Fried and Howard, 2000; Day, 2012), minimum *P-T* conditions of microdiamond precipitation can vary between 2.7 GPa/550°C (assuming the diamond-graphite transition by Fried and Howard, 2000) and 3.2 GPa/560°C (assuming the diamond-graphite transition by Kennedy and Kennedy, 1976) (Fig. 8). We consider the diamond-graphite transition curve by Fried and Howard (2000) as the most accurate one as it is based on the Gibbs free energy equation for carbon that fits experimental data over a large *P-T* range (Fried and Howard, 2000).

Based on mineralogical data (see supplementary information of Frezzotti et al. 2011), $f_{O_2}^{fluid/rock}$ should range between 1.5 $\log_{10}$ units above and 2 $\log_{10}$ units below the fayalite-magnetite-quartz buffer (i.e., FMQ–2 < $\log_{10} f_{O_2}$ < FMQ+1.5) at *P* = ~3.4 GPa and *T* = ~600°C. This range can be narrowed further if one considers the following: (1) the fluid phase must be H_2O rich, i.e. the fluid inclusions that are associated with microdiamonds are H_2O-rich without any Raman detectable CO_2 in the vapor phase. This constrains the mole fraction of CO_2 in the fluid phase to be < 0.026 (Diamond and Akinfiev, 2003). (2) CH_4 is not likely to be the dominant carbon-bearing fluid species due to the association of microdiamonds with carbonate mineral phases (Frezzotti et al., 2011).

Taking these constraints into consideration, GFluid calculations show that $\log_{10} f_{O_2}^{fluid/rock}$ is expected to range between ~FMQ–0.8 and ~FMQ+1.0 at 2.4 GPa/530°C, between ~FMQ–1.0 and ~FMQ+0.8 at 3.2 GPa/590°C, and between ~FMQ–1.1 and ~FMQ+1.0 at 4 GPa/600°C. Note that a different maximum pressure (i.e., 3.2 GPa at 590°C or 4 GPa at 600°C) does not significantly

change $f_{O_2}^{fluid/rock}$. Although $f_{O_2}^{fluid/rock}$ values are near those of FMQ, it does not necessarily imply that the change of $f_{O_2}^{fluid/rock}$ with *P*-*T* should, therefore, be parallel to the FMQ equilibrium curve. Rather, it indicates that, whichever $f_{O_2}^{fluid/rock}$ buffer is chosen, it should result in the given $f_{O_2}^{fluid/rock}$ range for the specified *P*-*T* conditions. For example, $f_{O_2}^{fluid/rock}$ could also be buffered by the enstatite-magnesite-olivine-diamond (EMOD) equilibrium. In that case, $\log_{10} f_{O_2}^{fluid/rock}$ would be between EMOD−1.4 and EMOD+0.3 at 2.4 GPa/530°C, between EMOD−1.2 and EMOD+0.6 at 3.2 GPa/590°C, and between EMOD−1.2 and EMOD+0.9 at 4 GPa/600°C (i.e., within the above defined range), where $f_{O_2}^{FMQ}$ and $f_{O_2}^{EMOD}$ were calculated using the following equations for FMQ (O'Neill, 1987; Ballhaus et al., 1991):

$$\log_{10} f_{O_2}^{FMQ} = 82.75+0.00484T_K-30681T_K-24.45\log_{10}T_K+94P_{kbar}/T_K-0.002P_{kbar} \quad (3)$$

and EMOD (Stagno and Frost, 2010):

$$\log_{10} f_{O_2}^{EMOD} = 5.14 - 21380/T_K + 0.078\,(P_{bar}-1)/\,T_K \quad (4)$$

The major difference between $f_{O_2}^{FMQ}$ and $f_{O_2}^{EMOD}$ is that with increasing *P* and *T*, $f_{O_2}^{EMOD}$ becomes more reduced relative to $f_{O_2}^{FMQ}$. As it is impossible to constrain the exact $f_{O_2}^{fluid/rock}$ buffer, we will use both the FMQ and EMOD equilibria to fix f_{O_2} in our calculations.

5.2.1. EMOD results

Figure 8 shows the results for the calculations assuming that $f_{O_2}^{fluid/rock} = f_{O_2}^{EMOD}$. Here, calculated *P*-*T* conditions at which the fluid is carbon saturated ($a_C^{fluid} = 1$) are shown for different X_C values (referred to as X_C isopleths). X_C is defined as follows:

$$X_C = n_C/(n_C+n_H)$$

518 where n_C and n_H denote the atomic carbon and hydrogen content of the fluid phase. For a H_2O-CO_2

519 mixture

520 $$n_C = X_{CO_2}^{fluid} \text{ and } n_H = 2\ X_{H_2O}^{fluid}$$

521 The mole fractions of CO_2, H_2O, and n_C in the fluid phase (assuming a H_2O-CO_2 fluid) can be

522 determined from X_C:

523 $$X_{H_2O}^{fluid} = (1 - X_C)/(X_C + 1) \quad (5)$$

524 $$X_{CO_2}^{fluid} = 2\ X_C /(X_C + 1) \quad (6)$$

525 $$n_C = 100\% \times 2\ X_C /3\ (X_C + 1) \quad (7)$$

526 A X_C increment value of 0.001 corresponds to a n_C change of ~0.07 mol.% (Eqn. 7).

527 Typically, X_C isopleths show decreasing values with increasing P at constant T (Fig. 8). A

528 fluid with an initial value of $X_C = 0.01$, that is exposed to P-T environment in which carbon-

529 saturated fluids have lower X_C values (i.e., P-T conditions on the high-pressure, low-temperature

530 side of the $X_C = 0.01$ isopleth, see Fig. 8), is carbon supersaturated. It is thus to be expected that

531 such a fluid will re-equilibrate to a carbon-saturated condition by means of graphite/diamond

532 precipitation during which the X_C value will drop to that of the carbon-saturated fluid.

533 A fluid with an initial X_C value of 0.01 that evolves along the P-T path of the Lago di

534 Cignana unit shows four stages related to graphite/diamond precipitation and graphite/diamond

535 dissolution (Fig. 8).

536

537 Stage I: between *a* and *b*: The fluid with $X_C = 0.01$ is in a P-T environment in which carbon-

538 saturated fluids have X_C values > 0.01, i.e. the fluid is carbon undersaturated and graphite

539 precipitation is not possible.

540

541 Stage II: between *b* and *c*: Here, the fluid is in a P-T environment in which carbon-saturated fluids

542 have X_C values less than 0.01 (i.e. from 0.01 at *b* to slightly below 0.004 at *c*). A C-O-H fluid with

543 X_C = 0.01 becomes thus carbon supersaturated as soon as it intersects X_C isopleths with values lower
544 than 0.01. In that case, the fluid will precipitate graphite and consequently the X_C value of the fluid
545 will drop. As the fluid progresses along the prograde *P-T* path, it will continuously precipitate
546 graphite while X_C is systematically decreasing. It is important to note that during prograde graphite
547 precipitation, the C-O-H fluid will always remain near carbon saturation. At point *c* the fluid has
548 reached a X_C value slightly below 0.004.
549
550 Stage III: between *c* and *d*: The fluid behaves the same as in stage II, with the exception that it now
551 precipitates diamond. At point *d* the fluid has reached a X_C value of 0.003.
552
553 Stage IV: beyond *d* (retrograde metamorphism): The *P-T* path now crosses X_C isopleths with
554 increasing values, i.e. the X_C value of the fluid (0.003) is smaller than that of the carbon-saturated
555 fluid and the fluid may (partially) dissolve diamond. As the X_C isopleths show increasing values
556 with decreasing pressure (Fig. 8), one would expect diamond to dissolve during retrograde
557 metamorphism. However, complete or partial diamond preservation during retrograde
558 metamorphism is possible if either the fluid-diamond ratio is low (i.e., there is not sufficient fluid
559 available to dissolve the complete diamond crystal) or there is simply no direct contact between the
560 fluid phase and diamond.
561 There is also the possibility that the X_C of the fluid phase may increase during retrograde
562 metamorphism as a result of H_2O removal from the C-O-H fluid by hydration reactions. In that
563 event the C-O-H fluid becomes carbon supersaturated and one may expect, depending on the *P-T*
564 conditions, retrograde diamond and/or graphite growth. In that case, one would expect poorly
565 crystalline diamond or graphite because of the carbon-supersaturated status of the fluid.
566 The fact that prograde graphite has not been observed implies that the fluid could not have
567 had high X_C values and must have been water rich. The maximum X_C value is constrained by the X_C
568 isopleth that crosses the *P-T* path where the diamond-graphite transition curve intersects the *P-T*

path. Any X_C value greater than this value should have resulted in prograde graphite precipitation. In this case, the maximum X_C value that the fluid could have had is slightly smaller than 0.004 ($X_{H_2O}^{fluid} > \sim 0.992$) assuming that $f_{O_2}^{fluid/rock}$ is fixed by the EMOD equilibrium (Fig. 8). Further, diamond precipitation is not possible if the fluid had a X_C value of 0.003 or less (i.e., $X_{H_2O}^{fluid} \geq 0.997$) as X_C isopleths with lower values do not intersect the *P-T* path (Fig. 8). In other words, $X_{CO_2}^{fluid}$ is constrained to be in between 0.008 and 0.003. Increasing $f_{O_2}^{fluid/rock}$ to EMOD+0.5 (still within the defined limits) will increase the X_C range to be in between 0.013 and 0.01 (i.e., $X_{CO_2}^{fluid}$ to be in between 0.017 and 0.026) (Fig. 9).

5.2.2. FMQ results

Figure 10 shows the results for the calculations assuming that $f_{O_2}^{fluid/rock} = f_{O_2}^{FMQ}$. Here, the X_C isopleths have an almost identical slope as the *P-T* path, which implies that neither graphite nor diamond precipitation can occur during prograde metamorphism as the prograde *P-T* path does not intersect X_C isopleths.

6. CONCLUSIONS

The garnetites from LCU (Western Alps, Italy) are the fist example of diamond formation from C-saturated oxidized C-O-H fluid phases at low temperatures during deep oceanic subduction. Since LCU diamonds were formed in oceanic sediments rich in H_2O and carbonates, their study allows us to model carbon transport during deep subduction to depths of around 100 km.

592 Formation of diamonds occurred at $P \geq 3.2$ GPa and about 600°C, when rock-buffered C-O-H
593 crustal fluid reached the excess concentration of C required for the spontaneous nucleation of
594 diamond. The association of minor (disordered) sp^2- with (ordered) sp^3-bonded carbon indicates
595 variable nucleation/crystallization kinetics, where disordered sp^2 carbon acted as a precursor for
596 diamond formation outside the thermodynamic stability field of crystalline graphite. At these low
597 temperatures, carbon precipitation from C-O-H fluids appears as the only viable mechanism for
598 diamond formation, since an origin by graphite conversion is impeded by the high kinetic barrier
599 necessary to break sp^2 bonds and to fix sp^3 C symmetry.

600 The crustal fluid phases from which diamond grew were water-rich with $0.997 > X_{H_2O}^{fluid} > \sim 0.992$
601 assuming that $f_{O_2}^{fluid/rock} = f_{O_2}^{EMOD}$. If the fluid were more CO_2 rich, then graphite would have
602 precipitated during the prograde stage of the *P-T* path. The exact values of $X_{H_2O}^{fluid}$ and the maximum
603 relative amount of diamond that can precipitate will change if either the *P-T* path up to 4 GPa or a
604 different graphite-diamond transition curve are chosen. However, these changes will not be
605 significant and the main conclusions will thus remain the same.

606 In UHPM rocks, the H_2O-enriched nature of crustal fluids responsible for diamond formation
607 has long been recognized (cf. Ogasawara et al., 2000; Castelli et al., 2007; and references therein).
608 Ogasawara et al. (2000) suggested a $0.01 < X_{CO_2}^{fluid} < 0.10$ for diamond-bearing rocks, and $X_{CO_2}^{fluid} <$
609 0.01 for rocks that lack diamonds at Kokchetav. Our thermodynamic modelling at variable *P-T-*
610 $f_{O_2}^{fluid/rock}$ conditions suggests that a very low $X_{CO_2}^{fluid}$ in diamond-forming fluids does not represent a
611 major constraint, as at LCU diamond formed in almost pure H_2O fluids ($X_{CO_2}^{fluid} < 0.01$). In this
612 respect the effect of carbonate dissolution could have an influence in raising the total amount of
613 carbon dissolved into H_2O-rich fluids.

614 Our modelling indicates that prograde diamond precipitation is only feasible if the rock *P-T*
615 path is steeper than the X_C isopleths of a carbon-saturated fluid in *P-T* space. The slope of the X_C

isopleths is steep if $f_{O_2}^{fluid/rock} = f_{O_2}^{FMQ}$, whereas it becomes flatter if $f_{O_2}^{fluid/rock}$ decreases (relative to $f_{O_2}^{FMQ}$) with depth (e.g., $f_{O_2}^{EMOD}$). In other words, diamond precipitation from C-O-H fluids during UHP metamorphism is controlled by the prograde *P*-*T* path and the change of $f_{O_2}^{fluid/rock}$ with depth.

Therefore, the most favourable conditions for microdiamond precipitation are (a) a water-rich C-O-H fluid, (b) a steep *P*-*T* path (i.e., a large $\Delta P/\Delta T$) and (c) a rapid decrease of $f_{O_2}^{fluid/rock}$ (relative to $f_{O_2}^{FMQ}$) with depth. A trend of decreasing $f_{O_2}^{fluid/rock}$ (relative to $f_{O_2}^{FMQ}$) with depth has been proposed in subduction zone environments (e.g., Malaspina and Tumiati, 2012). Generally, the minimum pressure at which carbon phases can precipitate from a C-O-H fluid along the prograde *P*-*T* path increases if the H_2O content of the fluid phase becomes greater (decreasing X_C values). Dehydration reactions during prograde metamorphism increase the H_2O content of the fluid phase and may thus favour diamond precipitation, whereas hydration reactions during retrograde metamorphism remove H_2O from the fluid phase and may cause the C-O-H fluid to become carbon supersaturated and stimulate precipitation of (poorly crystalline) diamond.

Acknowledgments

Thorough reviews by Larissa Dobrzhinetskaya and two anonymous reviewers, as well as careful editorial handling by M. Norman and W. Sun are gratefully acknowledged. We acknowledge M. Placidi for the fine technical assistance on Raman spectroscopy. This study was supported by Italian PRIN grant 2010PMKZX7, and by US NSF grant EAR 0911669. Raman facilities (2012) were provided by PNRA, the Italian agency for scientific research in Antarctica.

640

641 REFERENCES

642 Akaishi M. and Yamaoka H. (2000) Crystallization of diamond from C-O-H fluids under high-temperature
643 and high-pressure conditions: *J. Cryst. Growth* **209**, 999-1003.

644 Angiboust S., Agard P., Jolivet L. and Beyssac O. (2009) The Zermatt-Saas ophiolite: the largest (60-km
645 wide) and deepest (c. 70–80 km) continuous slice of oceanic lithosphere detached from a subduction
646 zone? *Terra Nova* **21**, 171–180.

647 Arima M., Kozai Y. and Akaishi M. (2002) Diamond nucleation and growth by reduction of carbonate melts
648 under high-pressure and high-temperature conditions. *Geology* **30**, 691-694.

649 Armbruster T. (1995) Structure refinement of hydrous andradite $Ca_3Fe_{1.54}Mn_{0.20}Al_{0.26}(SiO_4)_{1.65}(O_4H_4)_{1.35}$,
650 from the Wessels mine, Kalahari manganese field, South Africa. *Eur. J. Mineral.* **7**, 1221–1225.

651 Armbruster T. and Lager G.A. (1989) Oxygen disorder and the hydrogen position in garnet-hydrogarnet
652 solid solutions. *Eur. J. Mineral.* **1**, 363–369.

653 Baijot M., Hatert F. and Fransolet A.-M. (2011) Mineralogical and geochemical study of pseudocoticule
654 from the Stavelot Massif, Ardennes (Belgium), and redefinition of coticule. *Eur. J. Mineral.* **23**, 633-
655 644.

656 Ballhaus C., Berry R.F. and Green D.H. (1991) High pressure experimental calibration of the olivine-
657 orthopyroxene-spinel oxygen barometer: implications for the oxidation state of the upper mantle.
658 *Contrib. Mineral. Petrol.* **107**, 27-40.

659 Bearth P. (1967) Die Ophiolithe der Zone von Zermatt-Saas Fee. *Beiträge zur Geologischen Karte der*
660 *Schweitz, Neue Folge* **132**, 1-130.

661 Bersani D., Andò S., Vignola P., Moltifiori G., Marino I.G., Lottici P.P., et al. (2009) Micro-Raman
662 spectroscopy as a routine tool for garnet analysis. *Spectrochim. Acta A* **73**, 484-491.

663 Beyssac O., Goffé B., Petitet J.P., Froigneux E., Moreau M. and Rouzaud J.N. (2003) On the
664 characterization of disordered and heterogeneous carbonaceous materials using Raman spectroscopy.
665 *Spectrochim. Acta A* **59**, 2267–2276.

666 Birrell J., Gerbi J.E., Auciello O., Gibson J.M., Johnson J. and Carlisle J.A. (2005) Interpretation of the
667 Raman spectra of ultrananocrystalline diamond. *Diam. Relat. Mater.* **14,** 86-92.

668 Bostick B.C., Jones R.E., Ernst W.G., Chen C., Leech M. L. and Beane R.J. (2003) Low-temperature
669 microdiamond aggregates in the Maksyutov Metamorphic Complex, South Ural Mountains, Russia.
670 *Am. Mineral.* **88**, 1709-1717.

671 Bundy F.P. and Kasper, J.S. (1967) Hexagonal diamond - a new form of diamond. *J. Chem. Phys*. **46**, 3437-
672 3446.

673 Bureau H. and Keppler H. (1999) Complete miscibility between silicate melts and hydrous fluids in the
674 upper mantle; experimental evidence and geochemical implications. *Earth Planet. Sci. Lett.* **165**, 187-
675 196.

676 Cartigny P., de Corte K., Shatsky V.S., Ader M., De Paepe P., Sobolev N.V. and Javoy M. (2001) The origin
677 and formation of metamorphic microdiamonds from the Kokchetav massif, Kazakhstan: a nitrogen
678 and carbon isotopic study. *Chem. Geol.* **176**, 265-281.

679 Carswell D. A. and Compagnoni R. (2005) Introduction with review of the definition, distribution and
680 geotectonic significance of ultrahigh pressure metamorphism. In *Ultrahigh Pressure Metamorphism*
681 (eds. D.A. Carswell R. Compagnoni), *Eötvös University Press*, Budapest, pp. 3–9.

682 Castelli D., Rolfo F., Groppo C. and Compagnoni R. (2007) Impure marbles from the UHP Brossasco-Isasca
683 Unit (Dora-Maira Massif, Western Alps): evidence for Alpine equilibration in the diamond stability
684 field and evaluation of the $X(_{CO2})$ fluid evolution. *J. Metam. Geology* **25**, 587-603.

685 Compagnoni R., Rolfo, F. and Tamagno E. (2000) UHP Terranes in the Western Alps. *31st International*
686 *Geological Congress, Rio de Janeiro, Brazil*, 4 p, *CD geobr2000*, ISBN 85-901482-5-4. (Abstr.)

687 Dal Piaz G.V. (1974) Le métamorphisme de haute pression et basse température dans l'évolution structurale
688 du bassin ophiolitique alpino-apenninique. *Schweiz. mineral. petrograph. Mitt.* **54**, 399-424.

689 Dal Piaz G.V., Di Battistini G., Kienart J.-R. and Venturelli G. (1979) Manganiferous quartzitic schists of
690 the Piemonte ophiolite nappe in the Valsesia-Valtournanche area (Italian Western Alps). *Mem. Sci.*
691 *Geol. Padova* **32**, 1-24.

692 Day H.W. (2012) A revised diamond-graphite transition curve. *Am. Mineral*. **97**, 52–62.

693 De Corte K., Cartigny P., Shatsky V.S., Sobolev N.V. and Javoy M. (1998) Evidence of fluid inclusions in
694 metamorphic microdiamonds from the Kokchetav massif, northern Kazakhstan. *Geochim.*
695 *Cosmochim. Acta* **62**, 3765–3773.

696 De Corte K., Korsakov A., Taylor W.R., Cartigny P., Ader M. and De Paepe P. (2000) Diamond growth
697 during ultrahigh pressure metamorphism of the Kokchetav Massif, northern Kazakhstan. *Isl. Arc* **9**,
698 428–438.

699 Dewey, J.F., Helma M.L., Turco E., Hutton D.H.W. and Knott S.D. (1989) Kinematics of the western
700 Mediterranean. In *Alpine Tectonics* (eds. M.P. Coward D. Dietrich R.G. Park, R.G.) *Geological*
701 *Society Special Publication,* **45**, pp. 265–283.

702 Diamond L.W. and Akinfiev N.N. (2003) Solubility of CO_2 in water from 1.5 to 100 °C and from 0.1 to 100
703 MPa: evaluation of literature data and thermodynamic modelling. *Fluid Phase Equilibr.* **208**, 265-290.

704 Dobrzhinetskaya L.F. (2012) Microdiamonds - Frontier of ultrahigh-pressure metamorphism: A review.
705 *Gondwana Res.* **21**, 207-223.

706 Dobrzhinetskaya L.F., Braun T.V., Sheshkel G.G. and Podkuiko Y.A. (1994) Geology and structure of
707 diamond-bearing rocks of the Kokchetav massif (Kazakhstan). *Tectonophysics* **233**, 293–313.

708 Dobrzhinetskaya, L.F, Eide, E., Korneliussen, A., Larsen, R, Millege, J., Posukhova, T.V., Smith, D.S.,
709 Sturt, B.A., Taylor, W.R. and Tronnes, R. (1995) Diamond in metamorphic rocks of the Western
710 Gneiss Region in Norway. *Geology* **23**, 597–600.

711 Dobrzhinetskaya L.F., Green H.W., Mitchell T.E. and Dickerson, R.M. (2001) Metamorphic diamonds:
712 mechanism of growth and oxides inclusions. *Geology* **29**, 253–266.

713 Dobrzhinetskaya L.F., Green H.W., Bozhilov K.N., Mitchell T.E. and Dickerson R.M. (2003a)
714 Crystallization environment of Kazakhstan microdiamond: evidence from nanometric inclusions and
715 mineral associations. *J. Metam. Geol.* **21**, 425-437.

716 Dobrzhinetskaya L.F., Green H.W., Weschler M., Darus M., Wang Y.-C., Massonne H.-J. and Stöckhert B.
717 (2003b) Focused ion beam technique and transmission electron microscope studies of microdiamonds
718 from the Saxonian Erzgebirge, Germany. *Earth Planet. Sci. Lett.* **210**, 399-410.

719 Dobrzhinetskaya L.F., Wirth R. and Green H.W. (2005) Direct observation and analysis of a trapped COH
720 fluid growth medium in metamorphic diamond. *Terra Nova* **17**, 472-477.

721 Dobrzhinetskaya, L.F., Wirth, R. and Green, H.W. (2007) A look inside of diamond-forming media in deep
722 subduction zones. *PNAS* **104**, 9128-9132.

723 Eggler, D.H. and Baker, D.R. (1982) Reduced volatiles in the system C–O–H: implications to mantle
724 melting, fluid formation, and diamond genesis. In: *High Pressure Research in Geophysics* (eds. S.
725 Akimoto, M. Manghnani) Center for Academic Publications, Tokyo, p. 237–250.

726 Ferrando S., Frezzotti M.L., Dallai L. and Compagnoni R. (2005) Multiphase solid inclusions in UHP rocks
727 (Su-Lu, China): remnants of supercritical silicate-rich aqueous fluids released during continental
728 subduction. *Chem. Geol.* **223**, 68-81.

729 Ferrari A.C. and Robertson J. (2000) Interpretation of Raman Spectra of Disordered and Amorphous Carbon,
730 *Phys. Rev. B* **61**, 14095-14107.

731 Ferrari A.C. and Robertson J. (2001) Origin of the 1150-cm^{-1} Raman mode in nanocrystalline diamond.
732 *Phys. Rev. B* **63**, 121405.

733 Forster M., Lister G., Compagnoni R., Giles D., Hills Q., Betts P., Beltrando M. and Tamagno E. (2004)
734 Mapping of oceanic crust with “HP” to “UHP” metamorphism: The Lago di Cignana Unit (Western

735 Alps). In *Mapping Geology in Italy* (eds. G. Pasquarè C. Venturini G. Groppelli), APAT-
736 Dipartimento Difesa del Suolo – Servizio Geologico d'Italia, Roma 2004 (2006), Map 33, S.EL.CA. –
737 Firenze, pp. 279-286.

738 Foustoukos D.I. (2012) Metastable equilibrium in the C-H-O system: Graphite deposition in crustal fluids,
739 *Am. Mineral.* **97**, 1373-1380.

740 Frezzotti M.L., Di Vincenzo G., Ghezzo C. and Burke E.A.J. (1994) Evidence of magmatic CO_2 - rich fluids
741 in peraluminous graphite-bearing leucogranites from the Deep Freeze Range (Northern Victoria Land,
742 Antarctica*). Contrib. Mineral. Petrol.* **117**, 111-123.

743 Frezzotti M.L., Ferrando S., Dallai L. and Compagnoni R. (2007) Intermediate alkali-alumino-silicate
744 aqueous solutions released by deeply subducted continental crust: fluid evolution in UHP OH-rich
745 topaz-kyanite quartzites from Donghai (Sulu, China). *J. Petrol.* **48**, 1219-1241.

746 Frezzotti M.L., Selverstone J., Sharp Z.D. and Compagnoni R. (2011) Carbonate dissolution during
747 subduction revealed by diamond-bearing rocks from the Alps. *Nat. Geosci.* **4/10**, 703-706.

748 Frezzotti M.L., Tecce F. and Casagli. A. (2012a) Raman spectroscopy for fluid inclusion analysis. *J.*
749 *Geochem. Explor.* **112**, 1-20.

750 Frezzotti M.L., Ferrando S., Tecce F. and Castelli D. (2012b) Water content and nature of solutes in shallow-
751 mantle fluids from fluid inclusions. *Earth Planet. Sci. Lett.* **351**, 70-83.

752 Fried, L.E. and Howard, W.M. (2000) Explicit Gibbs free energy equation of state applied to the carbon
753 phase diagram. *Phys. Rev. B* **61**, 8734-8743.

754 Griffin W.L., O'Reilly S.Y. and Davies R.M. (2000) Subduction related diamond deposits? Constraints,
755 possibilities, and new data from Eastern Australia. *Rev. Econ. Geol.* **11**, 291–310.

756 Groppo C., Beltrando M. and Compagnoni R. (2009) P-T path of the UHP Lago di Cignana and adjoining
757 HP meta-ophiolitic units: insights into the evolution of the subducting Tethyan slab. *J. Metam. Geol.*
758 **27**, 207–231.

759 Hatch D.M. and Griffin D.T. (1989) Phase transitions in grandite garnets. *Am. Mineral.* **74**, 151–159.

760 Hemingway B.S., Bohlen S.R., Hankins W.B., Westrum E.R. Jr. and Kuskov O.L. (1998) Heat capacity and
761 thermodynamic properties for coesite and jadeite, reexamination of the quartz-coesite equilibrium
762 boundary *Am. Mineral.* **83**, 409–418,

763 Hofmeister A.M., Giesting P.A., Wopenka B., Gwanmesia G.D. and Jolliff, B.L. (2004) Vibrational
764 spectroscopy of pyrope-majorite garnets: Structural implications. *Am. Mineral.* **89**, 132-146.

765 Hwang S.L., Shen P., Chu H.T., Yui T.F. and Lin C.C. (2001) Genesis of microdiamonds from melt and
766 associated multiphase inclusions in garnet of ultrahigh-pressure gneiss from Erzgebirge, Germany.
767 *Earth Planet. Sci. Lett.* **188**, 9-15.

768 Hwang S.L., Shen P.Y, Yui T.F. and Chu H.T. (2003) Metal-sulfur-COH silicate fluid mediated diamond
769 nucleation in Kokchetav ultrahigh-pressure gneiss. *Eur. J. Mineral.* **15**, 503–511.

770 Irifune T., Kurio A., Sakamoto S., Inoue T. and Sumiya H. (2003) Ultrahard polycrystalline diamond from
771 graphite. *Nature* **421**, 599-600

772 Janák M., van Roermund H., Majka J., Gee. D.G. (2013) UHP metamorphism recorded by kyanite-bearing
773 eclogite in the Seve Nappe Complex of northern Jämtland, Swedish Caledonides. Gondwana Res. 23,
774 865–879. doi : 10.1016/j.gr.2012.06.012

775 Kagi H., Takahashi K., Hidaka H. and Masuda A. (1994) Chemical properties of Central African carbonado
776 and its genetic implication. *Geochim. Cosmochim. Acta* **58**, 2629–2638

777 Kennedy C.S. and Kennedy G.C. (1976) The equilibrium boundary between graphite and diamond. *J.*
778 *Geophys. Res.* **81**, 2467-2470.

779 Khokhryakov A.F., Nechaev D.V., Sokol A.G. and Pal'yanov Y.N. (2009) Formation of various types of
780 graphite inclusions in diamond: Experimental data. *Lithos* **112S**, 683–689.

King R.L., Bebout G.E., Kobayashi K., Nakamura E. and van der Klauw S.N.G.C. (2004) Ultrahigh-pressure metabasaltic garnets as probes into deep subduction zone chemical cycling. *Geochem. Geophys. Geosy.* **5**, Q12J14.

Kobayashi S. and Shoji T (1987) Infrared spectra and cell dimensions of hydrothermally synthesized grandite-hydrograndite series. *Mineral. J.* **13**, 490-499.

Kopylova M., Navon O., Dubrovinsky L. and Khachatryan G. (2010) Carbonatitic mineralogy of natural diamond-forming fluids. *Earth Planet. Sci. Lett.* **291**, 126-137.

Korsakov A.V. and Hermann J. (2006) Silicate and carbonate melt inclusions associated with diamonds in deeply subducted carbonate rocks. *Earth Planet. Sci. Lett.* **241**, 104-118.

Korsakov A.V., Shatsky V.S., Sobolev N.V. and Zayachkovsky A.A. (2002) Garnet-biotite-clinozoisite gneisses: a new type of diamondiferous metamorphic rocks of the Kokchetav Massif. *Eur. J. Mineral.* **14**, 915–929.

Korsakov A.V., Perraki M., Zedgenizov D.A., Bindi L., Vandenabeele P., Suzuki A. and Kagi H. (2010) Diamond-Graphite Relationships in Ultrahigh-pressure Metamorphic Rocks from the Kokchetav Massif, Northern Kazakhstan. *J. Petrol.* **51**, 763-783.Kotková, J., O'Brien, P.J. and Ziemann, M.A. (2011) Diamond and coesite discovered in Saxony-type granulite: solution to the Variscan garnet peridotite enigma. *Geology* **39**, 667–670.

Lager G.A., Armbruster T., Rotella F.J. and Rossman G.R. (1989) OH substitution in garnets: X-ray and neutron diffraction, infrared, and geometric-modeling studies. *Am. Mineral.* **74**, 840–851.

Lamens J., Geukens F., Viane W. (1986) Geological setting and genesis of coticules (spessartine metapelites) in the Lower Ordovician of the Stavelot Massif, Belgium. *J. Geol. Soc. London* **143**, 253–258.

Le Guillou C., Brunet F., Irifune T., Ohfuji H. and Rouzaud J.-N. (2007) Nanodiamond nucleation below 2273 K at 15 GPa from carbons with different structural organizations. *Carbon* **45**, 636–648.

804 Lespade P., Al-Jishi R. and Dresselhaus M.S. (1982) Model for Raman scattering from incompletely
805 graphitized carbons. *Carbon* **5**, 427–431.Li W.C., Chen R.X. and Zheng Y.F. (2013) Dehydration and
806 melting of diamond-bearing granitic orthogneiss during continental collision in the Sulu orogen. X
807 International Eclogite Conference, (Courmayeur, Italy, 2013) Abs. vol., p.77.
808 http://www.iec2013.unito.it/wpcontent/uploads/2013/07/abstract_volume.pdf

809 Lombardo B., Rubatto D. and Castelli D. (2002) Ion microprobe U-Pb dating of zircon from a Monviso
810 metaplagiogranite: implications for the evolution of the Piedmont-Liguria Tethys in the Western Alps.
811 *Ofioliti* **27**, 109–117.

812 Luque F.J., Ortega L., Barrenechea J.F., Millward D., Beyssac O., and Huizenga J.-M. (2009) Deposition of
813 highly crystalline graphite from moderate-temperature fluids. *Geology* **37**, 275–278.

814 Malaspina N., Poli S. and Fumagalli P. (2009) The oxidation state of metasomatized mantle wedge: insights
815 from C–O–H-bearing garnet peridotite. *J. Petrol.* **50**, 1533-1552.

816 Malaspina N. and Tumiati S. (2012) The role of C-O-H and oxygen fugacity in subduction-zone garnet
817 peridotites. *Eur. J. Mineral.* **24**, 607-618.

818 Manning C.E. (2004) The chemistry of subduction-zone fluids. *Earth Planet. Sci. Lett.* **223**, 1-16.

819 Massonne H.-J. (1999) A new occurrence of microdiamonds in quartzofeldspathic rocks of the Saxonian
820 Erzgebirge, Germany, and their metamorphic evolution. in *Proceedings of the 7th International*
821 *Kimberlite Conference, Cape Town, South Africa* (eds. J.J. Gurney, J.M. Gurney, M.D. Pascoe, S.H.
822 Richardson) Red Roof Design, Vol. **2**, pp 533–539.

823 Massonne, H-J. (2003) A comparison of the evolution of diamondiferous quartz-rich rocks from the
824 Saxonian Erzgebirge and the Kokchetav Massif: are so-called diamondiferous gneisses magmatic
825 rocks? *Earth Planet. Sci. Lett.* **216**, 347–364.

826 Mitura S. (2007) Nanodiamonds. *J. Achievements Materials and Manufacturing Engineering* **24**, 166-171.

827 Mitura S., Mitura K., Niedzielski P., Louda P. and Danilenko V. (2006) Nanocrystalline diamond, its
828 synthesis, properties and applications, *J. Achievements Materials and Manufacturing Engineering* **16**,
829 9-16.

830 Mposkos E.D. and Kostopoulos D.K. (2001) Diamond, former coesite and supersilicic garnet in
831 metasedimentary rocks from the Greek Rhodope: a new ultrahigh-pressure metamorphic province
832 established. *Earth Planet Sci Lett.* **192**, 497–506

833 Naemura, K., Ikuta, D., Kagi, H. et al. (2011) Diamond and other possible ultradeep evidence discovered in
834 the orogenic spinel-garnet peridotite from the Moldanubian Zone of the Bohemian Massif, Czech
835 Republic. In: L.F. Dobrzhinetskaya, S.W. Faryad, S. Wallis and S. Cuthbert (Eds.) *Ultrahigh Pressure*
836 *Metamorphism: 25 Years after Discovery of Coesite and Diamond*, 77–111, Elsevier, Amsterdam.

837 Nasdala L., Smith D.C., Kaindl R. and Ziemann M.A. (2004) Raman spectroscopy: analytical perspectives in
838 mineralogical research. In: *EMU notes in Mineralogy 6.* (eds. A. Beran, E. Libowitzky), European
839 Mineralogical Union, Wien, pp. 291-294.

840 O'Bannon E. F., Xia G., Green H. W., Wirth R. and Dobrzhinetskaya L. (2012) Experiments on
841 Graphitization of Diamond in the Presence of Water: Implications for Exhumation of Ultrahigh
842 Pressure Metamorphic Rocks. *AGU 2012 Fall Meeting* (San Francisco, USA 2012), abs.

843 Ogasawara Y., Ohta M., Fukasawa K., Katayama I. and Maruyama S. (2000) Diamond-bearing and
844 diamond-free metacarbonae rocks from Kumdy-kol in the Kokchetav Massif, northern Kazakhstan.
845 *Isl. Arc* **9**, 400-416.

846 Ogasawara Y. (2005) Microdiamonds in ultrahigh-pressure metamorphic rocks. *Elements* **1**, 91-96

847 Okada T., Utsumi W., Kaneko H., Turkevich V., Hamaya N. and Shimomura O. (2004) Kinetics of the
848 graphite–diamond transformation in aqueous fluid determined by in-situ X-ray diffractions at high
849 pressures and temperatures. *Phys. Chem. Miner.* **31**, 261-268.

850 O'Neill H.S.C. (1987) Quartz-fayalite-iron and quartz-fayalite-magnetite equilibria and the free energy
851 formation of fayalite (Fe_2SiO_4) and magnetite (Fe_3O_4). *Am. Mineral.* **72**, 67-75.

852 Orwa J.O., Nugent K.W., Jamieson D.N., Prawer S. (2000) Raman investigation of damage caused by deep
853 ion implantation in diamond. *Phys. Rev. B* **62**, 54615472.

854 Pal'yanov Y.N., Sokol A.G., Borzdov Y.M., Khokhryakov A. and Sobolev N.V. (1998) Crystallization of
855 diamond in the $CaCO_3$-C, $MgCO_3$-C and $CaMg(CO_3)_2$-C systems. *Dokl. Akad. Nauk.* **363**, 230-233.

856 Pal'yanov Y.N., Sokol A.G., Borzdov Y.M., Khokhryakov A.F. and Sobolev N.V. (2002a) Diamond
857 formation through carbonate-silicate interaction. *Am. Mineral.* **87**, 1009-1013.

858 Pal'yanov Y.N., Sokol A.G., Borzdov Y.M. and Khokhryakov A.F. (2002b) Fluid-bearing alkaline carbonate
859 melts as the medium for the formation of diamonds in the Earth's mantle: an experimental study.
860 *Lithos* **60**, 145-159.

861 Pal'yanov Y.N., Shatsky V.S., Sobolev N.V. and Sokol A.G. (2007) The role of mantle ultrapotassic fluids
862 in diamond formation. *PNAS* **104**, 9122-9127.

863 Parkinson C.D. and Katayama I. (1999a) Present day ultrahigh-pressure conditions of coesite inclusions in
864 zircon and garnet: Evidence from laser Raman microspectroscopy. *Geology* **27**, 979-982.

865 Parkinson C.D. and Katayama I. (1999b) Metamorphic microdiamond and coesite from Sulawesi, Indonesia:
866 evidence of deep subduction as SE Sundaland Margin. *EOS, Trans. Am. Geophys. Union*,Abs. vol.
867 F1181.

868 Perraki M., Proyer A., Mposkos E., Kaindl R. and Hoinkes G. (2006) Raman micro-spectroscopy on
869 diamond, graphite and other carbon polymorphs from the ultrahigh-pressure metamorphic Kimi
870 Complex of the Rhodope Metamorphic Province, NE Greece. *Earth Planet. Sci. Lett.* **241**, 672–685.

871 Petrovsky V.A., Shiryaev A.A., Lyutoev V.P., Sukharev A.E. and Martins M. (2010) Morphology and
872 defects of diamond grains in carbonado: clues to carbonado genesis. *Eur. J. Mineral.* **22**, 35-47.

873 Pleuger J., Roller S., Walter J.M., Jansen E. and Froitzheim N. (2007) Structural evolution of the contact
874 between two Penninic nappes (Zermatt-Saas zone and Combin zone, Western Alps) and implications
875 for the exhumation mechanism and paleogeography. *Int. J. Earth Sci.* **96**, 229–252.

876 Polino R., Dal Piaz, G.V. and Gosso G. (1990) Tectonic erosion at the Adria margin and accretionary
877 processes for the Cretaceous orogeny in the Alps. *Mém. Soc. Géol. France* **156**, 345–367.

878 Raimbourg H. and Kimura G. (2008) Non-lithostatic pressure in subduction zones. *Earth Planet. Sci. Lett.*
879 **274**, 414–422.

880 Reinecke T. (1991) Very-high-pressure metamorphism and uplift of coesite-bearing metasediments from the
881 Zermatt-Saas zone western Alps. *Eur. J. Mineral.* **3**, 7–17.

882 Reinecke T. (1998) Prograde high- to ultrahigh-pressure metamorphism and exhumation of oceanic
883 sediments at Lago di Cignana, Zermatt-Saas zone, Western Alps. *Lithos* **42**, 147-190.

884 Reinecke T., van der Klauw S.N.G.C. and Stöckhert B. (1994) UHP metamorphic oceanic crust of the
885 Zermatt-Saas zone (Piemontese zone) at Lago di Cignana, Valtournanche, Italy. In: *High Pressure*
886 *Metamorphism in the Western Alps. Guide-book to the field excursion B1* (eds. R. Compagnoni, B.
887 Messiga, D. Castelli) *16th General Meeting of the Intern. Mineral. Ass.*, 10–15 September, Pisa,
888 Ovidiografica, Pino Torinese, p. 117–126.

889 Roy D., Chhowalla M., Wang H., Sano N., Alexandrou I., Clyne T.W. and Amaratunga G.A.J. (2003)
890 Characterisation of Carbon Nano-Onions Using Raman Spectroscopy, *Chem. Phys. Lett.* **373**, 52-56.

891 Sato K., Akaishi M. and Yamaoka S. (1999) Spontaneous nucleation of diamond in the system $MgCO_3$-
892 $CaCO_3$-C at 7.7 GPa. *Diamond Relat. Mater*. **8**, 1900-1905.

893 Schertl H.-P. and Sobolev N.V. (2012) The Kokchetav massif, Kazakhstan: "Type locality" of diamond-
894 bearing UHP metamorphic rocks. *J. Asian Earth Sci.*, doi: 10.1016/j.jseaes.2012.10.032

895 Shatsky V.S., Sobolev N.V. and Vavilov M.A. (1995) Diamond-bearing rocks of the Kokchetav massif. In:
896 *Ultrahigh Pressure Metamorphism.* (eds. R.G. Coleman, X. Wang), Cambridge Academic Press,
897 Cambridge, New York, Melbourne, pp. 427–455.

898 Shatsky V., Zedgenizov E., Yefimova E., Rylov G., De Corte K. and Sobolev N. (2000) A comparison of
899 morphology and physical properties of microdiamonds from the mantle and crustal environments. In:

The P.H. Nixon Volume. Proceedings of 7th International Kimberlite Conference. (eds. J.J. Gurney , J.L. Gurney, M.D. Pascoe, S.H. Richardson), Red Roof Design CC, Capetown, pp. 757–763.

Schreyer W., Bernhardt H.-J. and Medenbach O. (1992) Petrologic evidence for a rhodochrosite precursor of spessartine in coticules of the Venn-Stavelot Massif, Belgium. *Mineral. Mag.* **56**, 527–532.

Schmidt S., Nagel T.J. and Froitzheim N. (2010) A new occurrence of microdiamond-bearing metamorphic rocks, SW Rhodopes, Greece. *Eur. J. Mineral.* **22**, 189–198.

Sitnikova E.S. and Shatsky V.S. (2009) New data of FTIR spectroscopy on the composition of diamond crystallization medium in metamorphic rocks of the Kokchetav massif. *Geol. Geophys.* **50**, 1095-1103 (in Russian).

Smith D.C. and Godard G. (2009) UV and VIS Raman spectra of natural lonsdaleites: towards a recognized standard. *Spectrochim. Acta A* **73A**, 428-435.

Smith D.C., Dobrzhinetskaya L.F., Godard G. and Green H.W. (2011) Diamond–lonsdaleite–graphite relations examined by Raman mapping of carbon microinclusions inside zircon at Kumdy Kol, Kokchetav, Kazakhstan: evidence of the metamictization of diamond. In: *Ultrahigh-Pressure Metamorphism: 25 Years After The Discovery of Coesite and Diamond* (eds. L.F. Dobrzhinetskaya, S.W. Faryad, S. Wallis, S. Cuthbert) Elsevier, London, pp. 44–111.

Smith D.C. and Godard G. (2013) A Raman spectroscopic study of diamond and disordered sp3-carbon in the coesite-bearing Straumen Eclogite Pod, Norway. *J. Metamor. Geol.* **31**, 19–33.

Sobolev N.V. and Shatsky V.S. (1990) Diamond inclusions in garnets from metamorphic rocks: a new environment for diamond formation. *Nature* **343**, 742–746.

Sokol A.G. and Pal'yanov Y.N. (2004) Diamond crystallization in fluid and carbonate-fluid systems under mantle P-T conditions; 2, An analytical review of experimental data. *Geochem. Int.* **42**, 1018-1032.

Sokol A.G., Tomilenko A.A., Pal'yanov Y.N., Borzdov Y.M., Pal'yanova G.A. and Khokhryakov AF (2000) Fluid regime of diamond crystallisation in carbonate-carbon systems. *Eur. J. Mineral.* **12**, 367-375.

924 Sokol A.G., Borzdov Y.M., Pal'yanov Y.N., Khokhryakov A.F. and Sobolev N.V. (2001) An experimental
925 demonstration of diamond formation in the dolomite-carbon and dolomite-fluid-carbon systems. *Eur.*
926 *J. Mineral.* **13**, 893-900.

927 Sokol A.G., Pal'yanov Y.N., Pal'yanova G.A. and Tomilenko A.A. (2004) Diamond crystallization in fluid
928 and carbonate-fluid systems under mantle P-T conditions; 1, Fluid composition. *Geochem. Int.* **42**,
929 830-838.

930 Spivak A.V. and Litvin Yu.A. (2004) Diamond syntheses in multi-component carbonate-carbon melts of
931 natural chemistry: Elementary processes and properties. *Diamond Relat. Mater.* **13**, 482-487.

932 Stagno V. and Frost D.J. (2010) Carbon speciation in the asthenosphere: Experimental measurements of the
933 redox conditions at which carbonate-bearing melts coexist with graphite or diamond in peridotite
934 assemblages. *Earth Planet. Sci. Lett.* **300**, 72-84.

935 Stöckhert B., Duyster J., Trepmann C. and Massonne H.-J. (2001) Microdiamond daughter crystals
936 precipitated from supercritical COH silicate fluids included in garnet, Erzgebirge, Germany. *Geology*
937 **29**, 391–394.

938 Tuinstra F. and Koenig J.L. (1970) Raman spectrum of graphite. *J. Chem. Phys.* **53**, 1126.

939 van der Klauw S.N.G.C., Reinecke T. and Stöckhert B. (1997) Exhumation of ultrahigh-pressure
940 metamorphic oceanic crust from Lago di Cignana, Piemontese zone, western Alps: the structural
941 record in metabasites. *Lithos* **41**, 79–102.

942 van Roermund H.L.M., Carswell D.A., Drury M.R. and Heijboer T.C. (2002) Microdiamonds in a
943 megacrystic garnet-websterite pod from Bardane on the island of Fjortoft, Western Norway. *Geology*
944 **30**, 959-962.

945 Vrijmoed J.C., Smith D.C. and van Roermund H.L.M. (2008) Raman confirmation of microdiamond in the
946 Svartberget Fe-Ti type garnet peridotite, Western Gneiss Region, Western Norway. *Terra Nova* **20**,
947 295-301.

948 Vrijmoed J.C., Van Roermund H.L. M. and Davies G.R. (2006) Evidence for diamond-grade ultra-high
949 pressure metamorphism and fluid interaction in the Svartberget Fe-Ti garnet peridotite-websterite
950 body, Western Gneiss Region, Norway. *Mineral. Petrol.* **88**, 381-405.

951 Wada N. and Solin S.A. (1981) Raman efficiency measurements of graphite. *Physica B+C* **105**, 353-356.

952 Watanabe H., Kume H., Mizuochi N., Yamasaki S., Kanno S. and Okushi, H. (2006) Nitrogen incorporation
953 in a homoepitaxial thin film. *Diamond Relat. Mater.* **15**, 554–558.

954 Wopenka B. and Pasteris J.D. (1993) Structural characterization of kerogens to granulite-facies graphite:
955 Applicability of Raman microprobe spectroscopy: *Am. Mineral.* **78**, 533-557.

956 Wu B.R. (2007) Structural and vibrational properties of the 6H diamond: first principles study. *Diamond*
957 *Relat. Mater.* **16**, 21-28.

958 Wu B.R. and Xu J.A. (1998) Total energy calculations of the lattice properties of cubic and hexagonal
959 diamond. *Phys. Rev. B* **57**, 13355-13358.

960 Xia G., O'Bannon E., Shi F., Green H.W. II1, Wirth R. and Dobrzhinetskaya L. (2013). Metastable
961 hydrocarbon formation during diamond-to- graphite transformation in presence of fluid. *GSA 2013*
962 *Meeting* (Denver, USA 2013), Abs. Vol.

963 Xu S.-T., Okay A.I., Ji S.-Y., Sengor A.M.C., Su W., Liu Y.-C. and Jiang L.-L. (1992) Diamond from the
964 Dabie Shan metamorphic rocks and its implication for tectonic setting. *Science* **256**, 80–82.

965 Yamato P., Agard P., Burov E., Le Pourhiet L., Jolivet L. and Tiberi C. (2007) Burial and exhumation in a
966 subduction wedge: Mutual constraints from thermomechanical modeling and natural P-T-t data
967 (Schistes Lustrés, western Alps). *J. Geophys. Res.-Sol. Ea.* **112**, B07410.

968 Yang J., Xu Z., Dobrzhinetskaya L.F., Green H.W., Pei X., Shi R., Wu C., Wooden J.L., Zhang J., Wan Y.,
969 Li H. (2003) Discovery of metamorphic diamonds in central China: An indication of a >4000-km-long
970 zone of deep subduction resulting from multiple continental collisions: *Terra Nova* **15**, 370–379,
971 doi:10.1046/j.1365-3121.2003.00511.x.

Zaitsev M. (2001) *Optical Properties of Diamond: a Data Handbook*, Springer-Verlag, Berlin, pp. 102–114.

Zhang, C. and Duan Z. (2009) A model for C-O-H fluid in the Earth's mantle. *Geochim. Cosmochim. Acta* **73**, 2089-2102.

Zhang C. and Duan Z. (2010) G-Fluid: An Excel spreadsheet for investigating C-O-H fluid composition under high temperatures and pressures. *Comput. Geosci.* **36**, 569-572.

CAPTIONS TO FIGURES

Fig. 1 – (**a**) Simplified tectonic sketch-map of the Italian Western Alps. Helvetic Domain: Mont Blanc-Aiguilles Rouges (MB); Penninic Domain: Grand St Bernard Zone (SB), and Monte Rosa (MR), Gran Paradiso (GP), Dora-Maira (DM) Internal Crystalline Massifs; the Piemonte Zone of Calc-schists with meta-ophiolites is shown in light (calc-schists) and dark grey (meta-ophiolites), respectively; Austroalpine Domain: Dent Blanche nappe (DB), Sesia–Lanzo Zone (SZ); Southern Alps (SA). The Lago di Cignana region is shown by a white arrow. (**b**) Geological map of the Lago di Cignana region (modified after Groppo et al., 2009; Compagnoni et al., 2000; Forster et al., 2004; Pleuger et al., 2007). Austroalpine Domain (Dent Blanche Nappe): (1) Valpelline Series; (2) Roisan Zone; (3) Arolla Series. Pennine Domain (Piemonte Zone): (4) Combin Zone; (5) Panchérot – Cime Bianche – Bettaforca Unit; (6) Zermatt–Saas Zone serpentinite; (7) Coesite- eclogite and metasediment (Lago di Cignana Unit); (8) Zermatt–Saas Zone eclogite and metagabbro. The white star indicates the location of the studied samples.

Fig. 2 - Microphotographs of diamonds and other inclusions in garnet. **a**) Bands of secondary quartz separating clusters of euhedral spessartine grains. **b**) Detail of spessartine (red square in Fig. 2a) showing the association of two cuboidal diamonds (Dmd) with magnesite (Mgs) and fluid inclusions (Flincs).

Fig. 3 - Microphotographs of diamonds in, and associated with, fluid inclusions. **a**) Diamond (Dmd) and calcite (Cc) inside a water-rich fluid inclusion. Diamonds are observed also outside the fluid inclusion along with magnesite (Mgs). **b**) Octahedral diamonds attached to fluid inclusions. **c**) Three diamonds associated with fluid inclusions. Note also the presence of numerous quartz (Qtz) and magnesite inclusions. **d**) Diamond inside a decrepitated (i.e., empty) fluid inclusion.

Fig. 4 - Raman spectra of diamond in garnet. **a**) First order band of diamond (Dmd). **b**) Graphite-like amorphous carbon (C) bands and the symmetric stretching band of the CO_3 group in carbonates in diamond spectrum. **c**) Symmetric stretching band of the CO_3 group in carbonates in diamond spectrum. Asterisks indicate host-garnet peaks.

Fig. 5 - Raman spectra of diamonds and other daughter phases in fluid inclusions. **a**) Association of diamond (Dmd), Mg-calcite (Mg-Cc), dawsonite (Daw) and rutile (Rt) in a H_2O-rich fluid inclusion. b) Association of diamond (Dmd), carbonate, graphite-like amorphous carbon (C) and rutile (Rt) in a H_2O-rich fluid inclusion. Note the absence of CO_2 in both spectra (bands predicted at 1280 and 1385 cm^{-1}). Asterisks indicate host-garnet peaks.

Fig. 6 - Sp^3-, and sp^2-bonded carbon in Raman spectra of diamond contained in fluid inclusions (laser excitation 514 nm). **a** and **b**) diamond (Dmd) spectrum showing the presence of additional sp^2-bonded carbon as hydrogenated carbon chains (CH) and as graphite-like amorphous carbon (C). Note also the occurrence of the symmetric stretching band of the CO_3 group in carbonates at 1077-1082 cm^{-1}. **c**) Diamond and graphite-like amorphous

carbon (C) in a decrepitated fluid inclusion. **d**) Diamond and graphite-like amorphous carbon in a fluid inclusion from sample ALC2, where microdiamonds are absent in garnet. The diamond band lies at 1328 cm^{-1} and shows a significant decrease in intensity and increase in FWHM (full width at half peak maximum intensity). These effects are indicative of presence of defects in diamonds, see text for discussion. Additional features include the presence of two bands at 1285 and 1305 cm^{-1}, tentatively assigned to and of a carbonate band at 1085 cm^{-1}. Asterisks indicate host-garnet peaks.

Fig. 7 – Raman mapping of progressive hardening of A_{1g} modes in garnet approaching diamonds, carbonates, quartz, and fluid inclusions. **a**) Microphotograph in plane polarized light of the mapped area in garnet over 50x45 µm. Diamond (Dmd), magnesite (Mgs), quartz (Qtz), and fluid inclusions (flincs) are indicated. **b**) Raman map of the variation of the intensity ratio of the two bands at 906 (A_{1g} mode) and 848 (T_{1g} mode) cm^{-1}. The ratio of I_{906}/I_{848} is about 0.4 in analyzed spessartine, and increases linearly from 1 until about 5-6, at a distance varying from 8 to 2 microns approaching the inclusions. The colors (see right side) indicate the I_{906}/I_{848} ratio. c) Spectra of garnet far from the inclusions (red) and in the proximity of fluid inclusions (blue). Main A_{1g} garnet modes are indicated. Asterisk corresponds to calcite band from the fluid inclusion.

Fig. 8 - *P-T* diagram showing X_C isopleths for a carbon-saturated C-O-H fluid in which $f_{O_2}^{fluid/rock} = f_{O_2}^{EMOD}$. Different stages (a, b, c, d) of graphite/diamond precipitation and graphite/diamond dissolution along the prograde *P-T* path of the Lago di Cignana (solid grey line, dashed grey line represents same *P-T* path extended to ~4.0 GPa) are discussed in the text. Graphite-diamond equilibrium curves after Fried and Howard (2000) (solid line), Kennedy and Kennedy (dotted line), and Day (2012) (dashed line) are indicated. The quartz-coesite equilibrium curve is after Hemingway et al. (1998).

1042 Fig. 9 - *P-T* diagram showing X_C isopleths for a carbon-saturated C-O-H fluid in which $f_{O_2}^{fluid/rock}$ is

1043 0.5 log10 units greater than $f_{O_2}^{EMOD}$ superimposed on the *P-T* path for the Lago di Cignana

1044 unit. See Fig. 8 for details on mineral reaction curves.

1045 Fig. 10 - *P-T* diagram showing X_C isopleths for a carbon-saturated C-O-H fluid in which $f_{O_2}^{fluid/rock}$ =

1046 $f_{O_2}^{FMQ}$ superimposed on the *P-T* path for the Lago di Cignana unit. See Fig. 8 for details on

1047 mineral reaction curves.

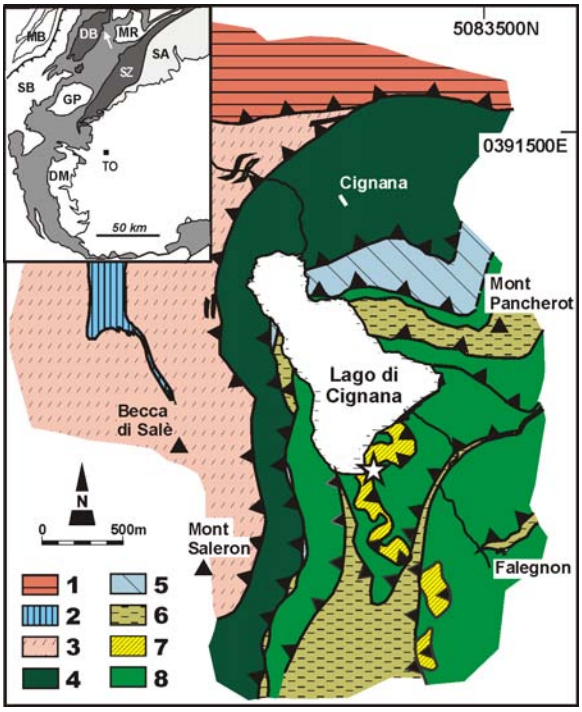
MB
DB
MR
SA
SZ
SB
GP
TO
DM
50 km
5083500N
0391500E
Cignana
Mont
Pancherot
Lago di
Cignana
Becca
di Salè
N
0
500m
Mont
Saleron
Falegnon
1
2
3
4
5
6
7
8

Fig. 1

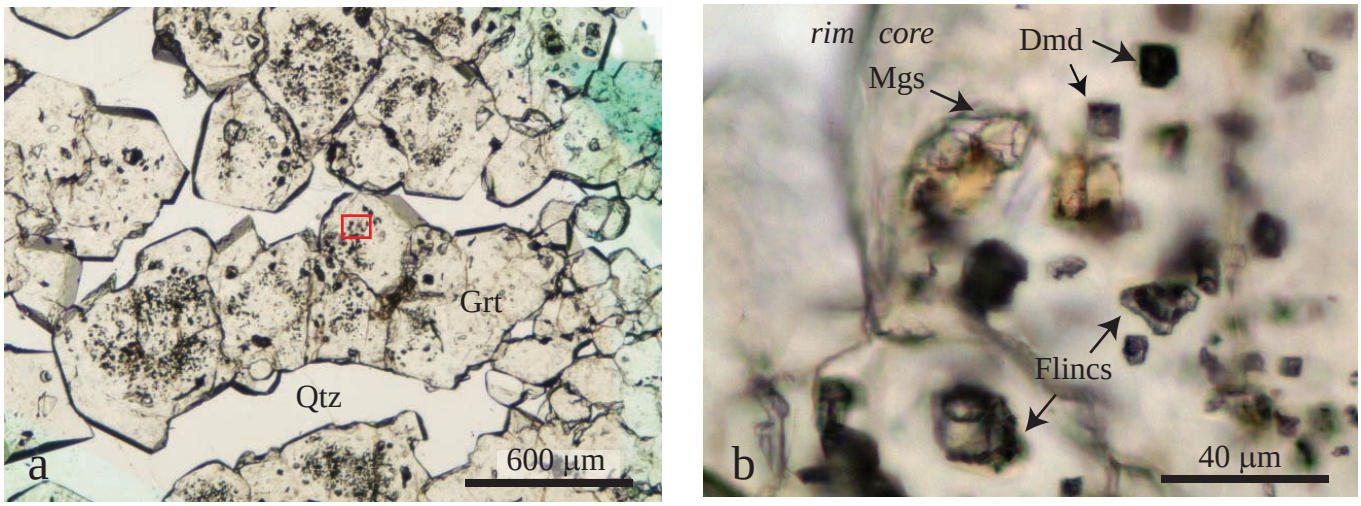

Fig. 2

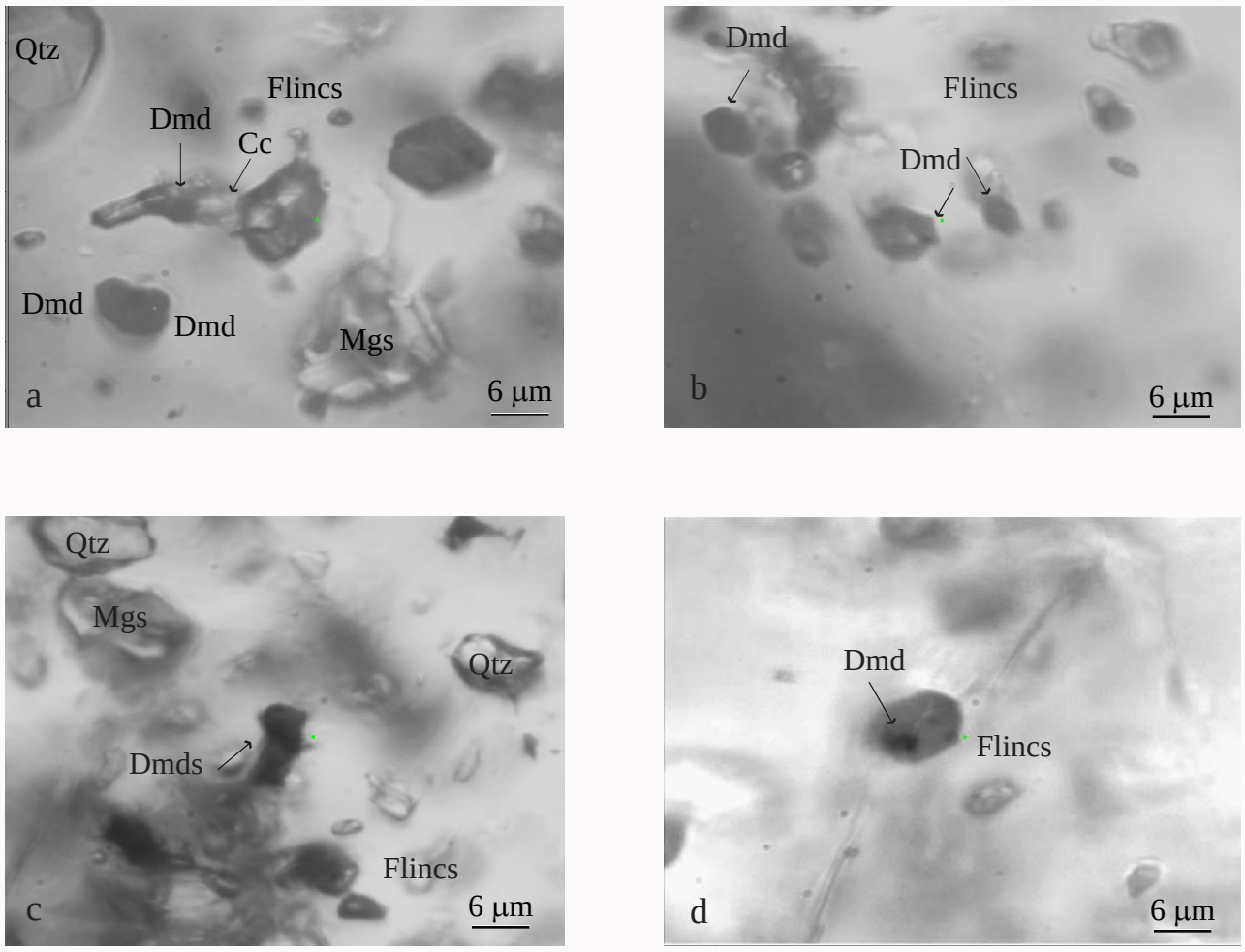
Qtz
Flincs
Dmd
Cc
Dmd
Dmd
Mgs
a
6 µm
Dmd
Flincs
Dmd
b
6 µm
Qtz
Mgs
Qtz
Dmds
Flincs
c
6 µm
Dmd
Flincs
d
6 µm

Fig. 3

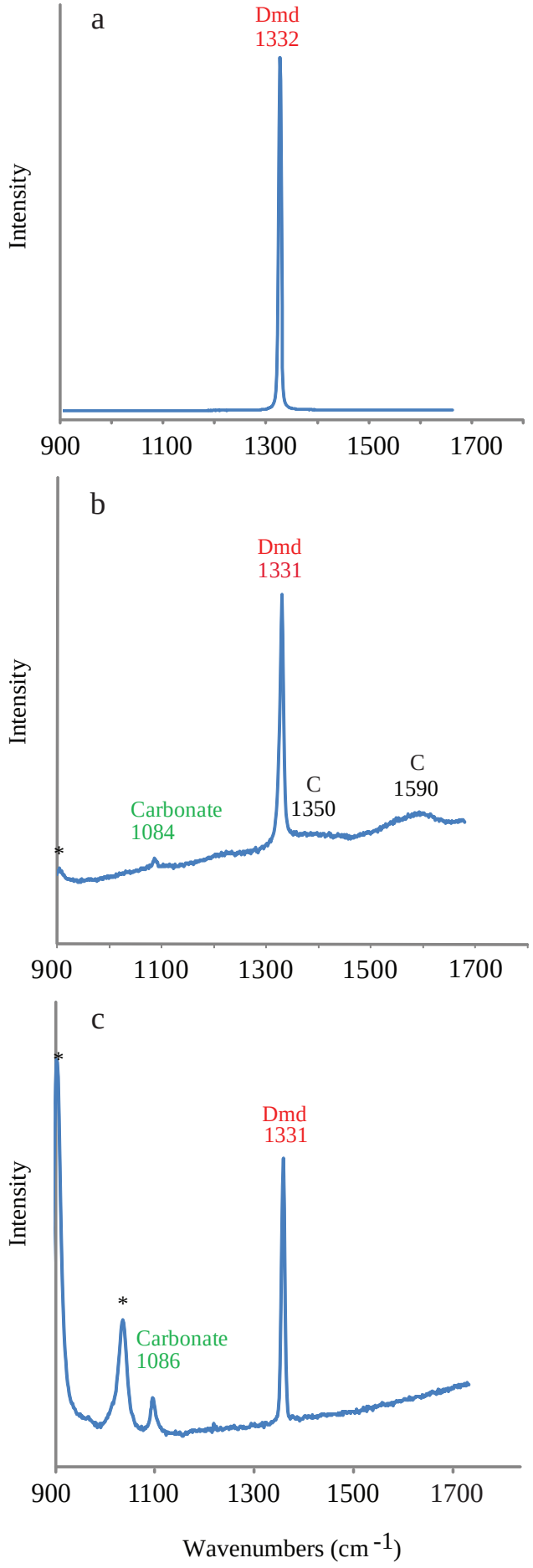
a
Dmd
1332
Intensity
900
1100
1300
1500
1700
b
Dmd
1331
C
1350
C
1590
Carbonate
1084
*
Intensity
900
1100
1300
1500
1700
c
*
Dmd
1331
*
Carbonate
1086
Intensity
900
1100
1300
1500
1700
Wavenumbers (cm -1)

Fig. 4

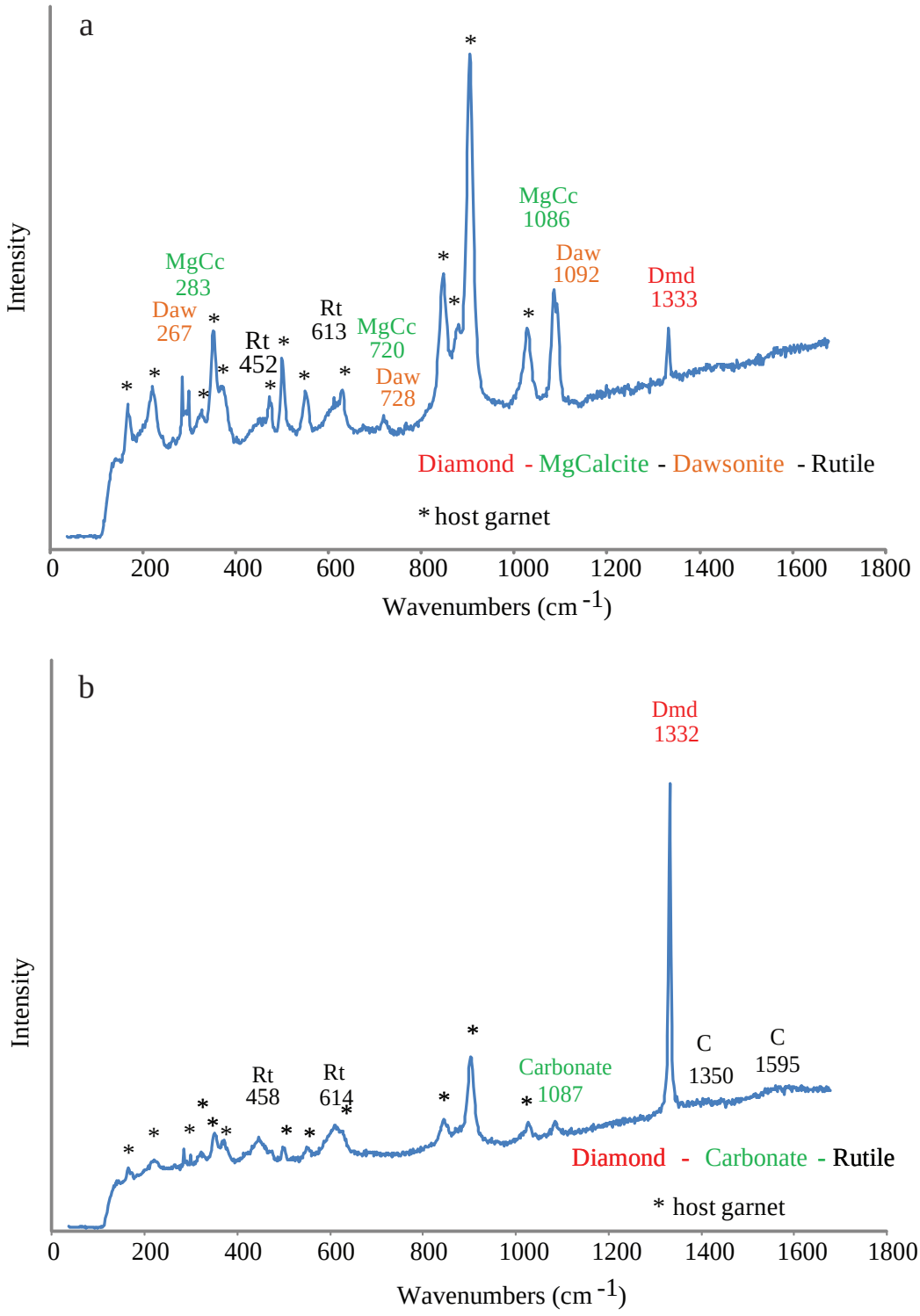
a
Intensity
MgCc
283
Daw
267
Rt
452
Rt
613
MgCc
720
Daw
728
MgCc
1086
Daw
1092
Dmd
1333
Diamond - MgCalcite - Dawsonite - Rutile
* host garnet
0
200
400
600
800
1000
1200
1400
1600
1800
Wavenumbers (cm -1)
b
Intensity
Dmd
1332
Rt
458
Rt
614
Carbonate
1087
C
1350
C
1595
Diamond - Carbonate - Rutile
* host garnet
0
200
400
600
800
1000
1200
1400
1600
1800
Wavenumbers (cm -1)

Fig. 5

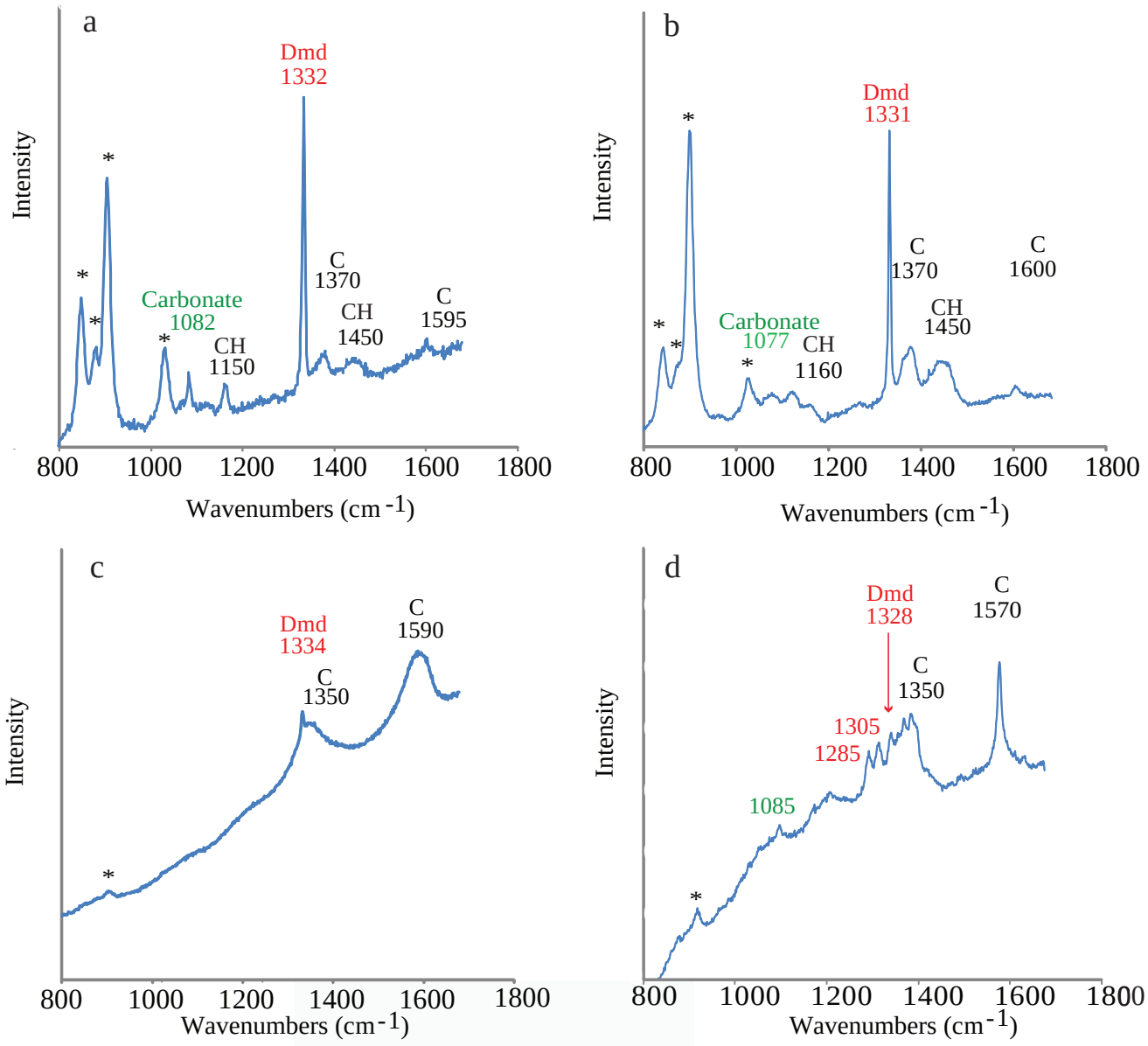
a
Intensity
Dmd
1332
C
1370
Carbonate
1082
CH
1150
CH
1450
C
1595
800
1000
1200
1400
1600
1800
Wavenumbers (cm -1)
b
Intensity
Dmd
1331
C
1370
C
1600
Carbonate
1077
CH
1160
CH
1450
800
1000
1200
1400
1600
1800
Wavenumbers (cm -1)
c
Intensity
Dmd
1334
C
1590
C
1350
800
1000
1200
1400
1600
1800
Wavenumbers (cm -1)
d
Intensity
Dmd
1328
C
1570
C
1350
1305
1285
1085
800
1000
1200
1400
1600
1800
Wavenumbers (cm -1)

Fig. 6

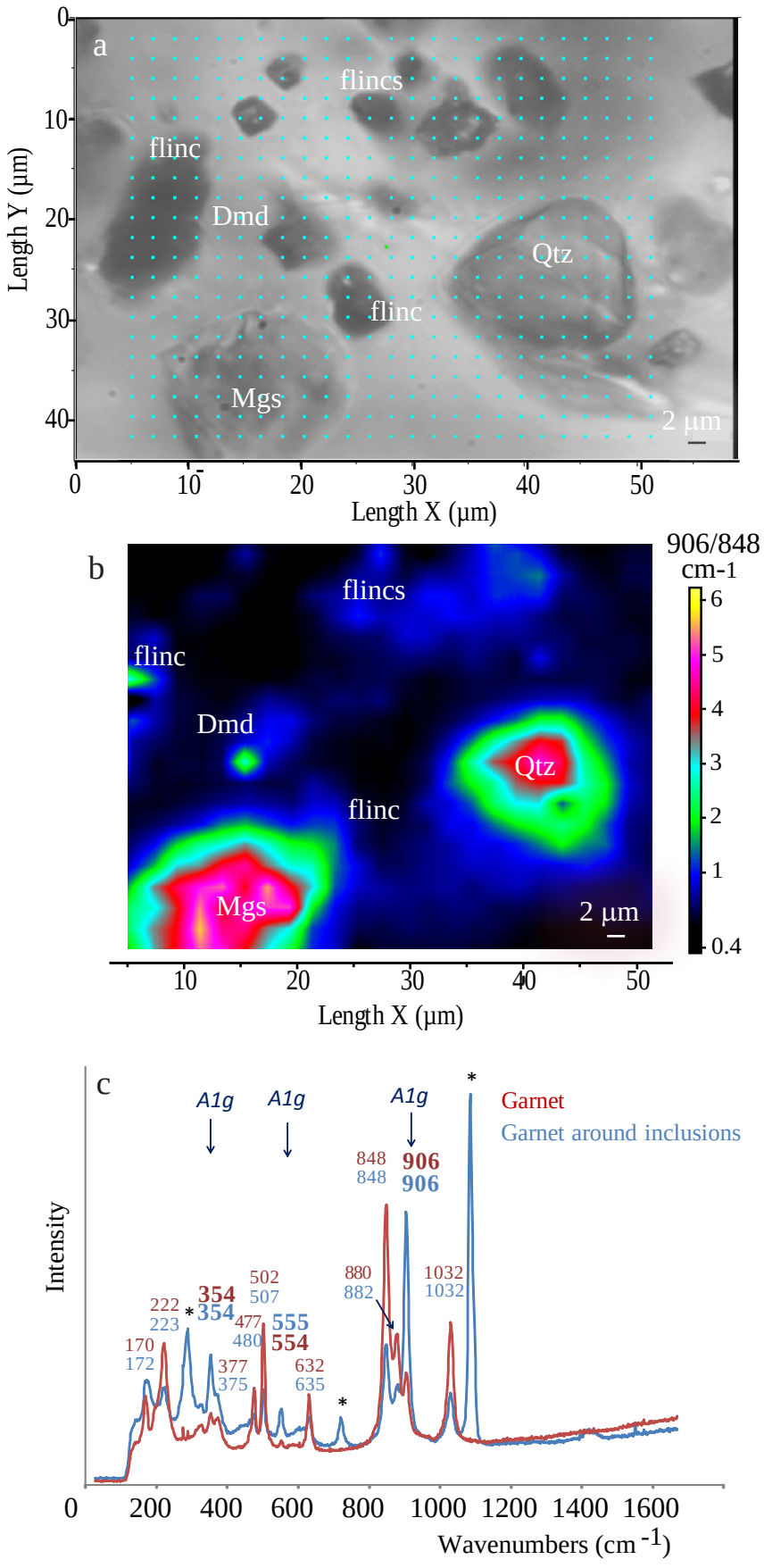
a
flincs
flinc
Dmd
Qtz
flinc
Mgs
2 µm
Length Y (µm)
Length X (µm)
b
flincs
flinc
Dmd
Qtz
flinc
Mgs
2 µm
906/848
cm-1
Length X (µm)
c
A1g
A1g
A1g
Garnet
Garnet around inclusions
848
848
906
906
880
882
1032
1032
502
507
354
354
222
223
477
480
555
554
170
172
377
375
632
635
Intensity
Wavenumbers (cm -1)

Fig. 7

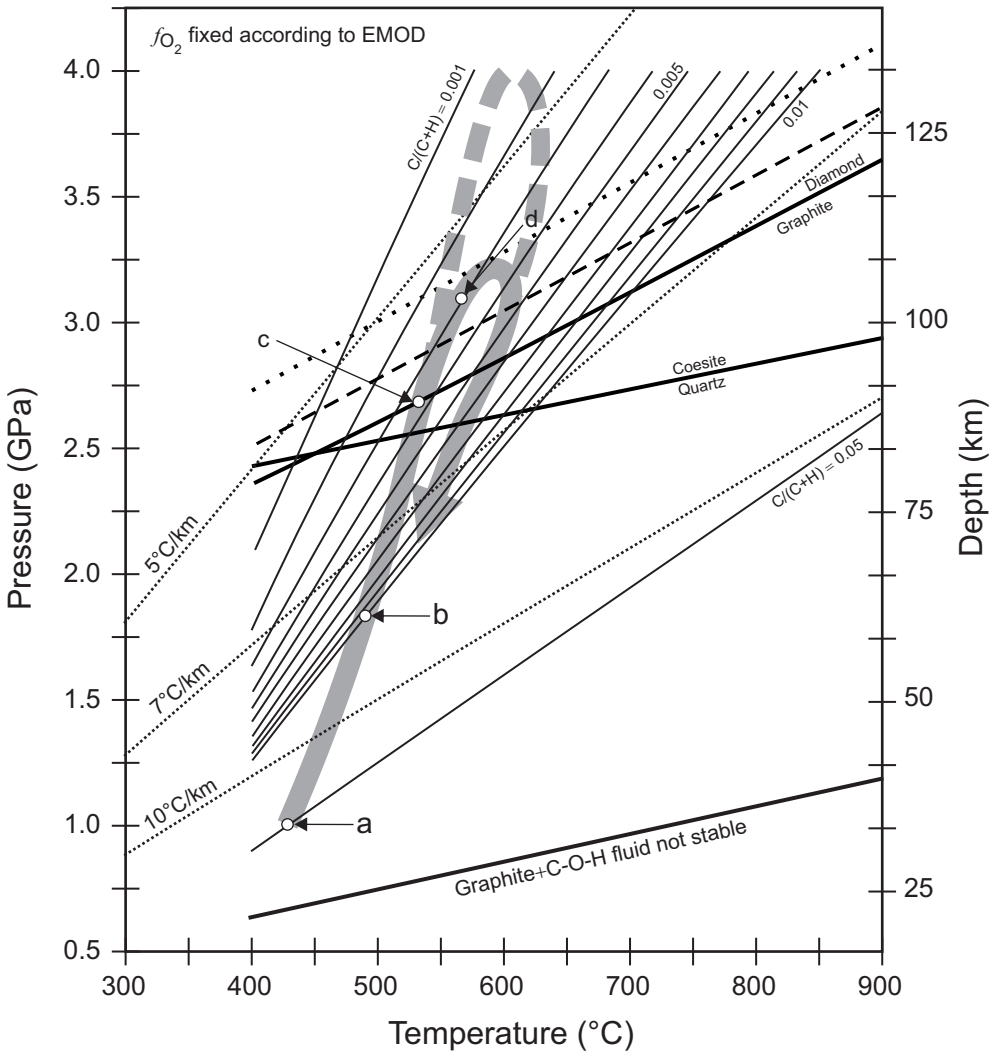
fO_2 fixed according to EMOD
C/(C+H) = 0.001
0.005
0.01
Diamond
Graphite
Coesite
Quartz
C/(C+H) = 0.05
5°C/km
7°C/km
10°C/km
a
b
c
d
Graphite+C-O-H fluid not stable
Pressure (GPa)
Depth (km)
Temperature (°C)
4.0
3.5
3.0
2.5
2.0
1.5
1.0
0.5
125
100
75
50
25
300
400
500
600
700
800
900

Fig. 8

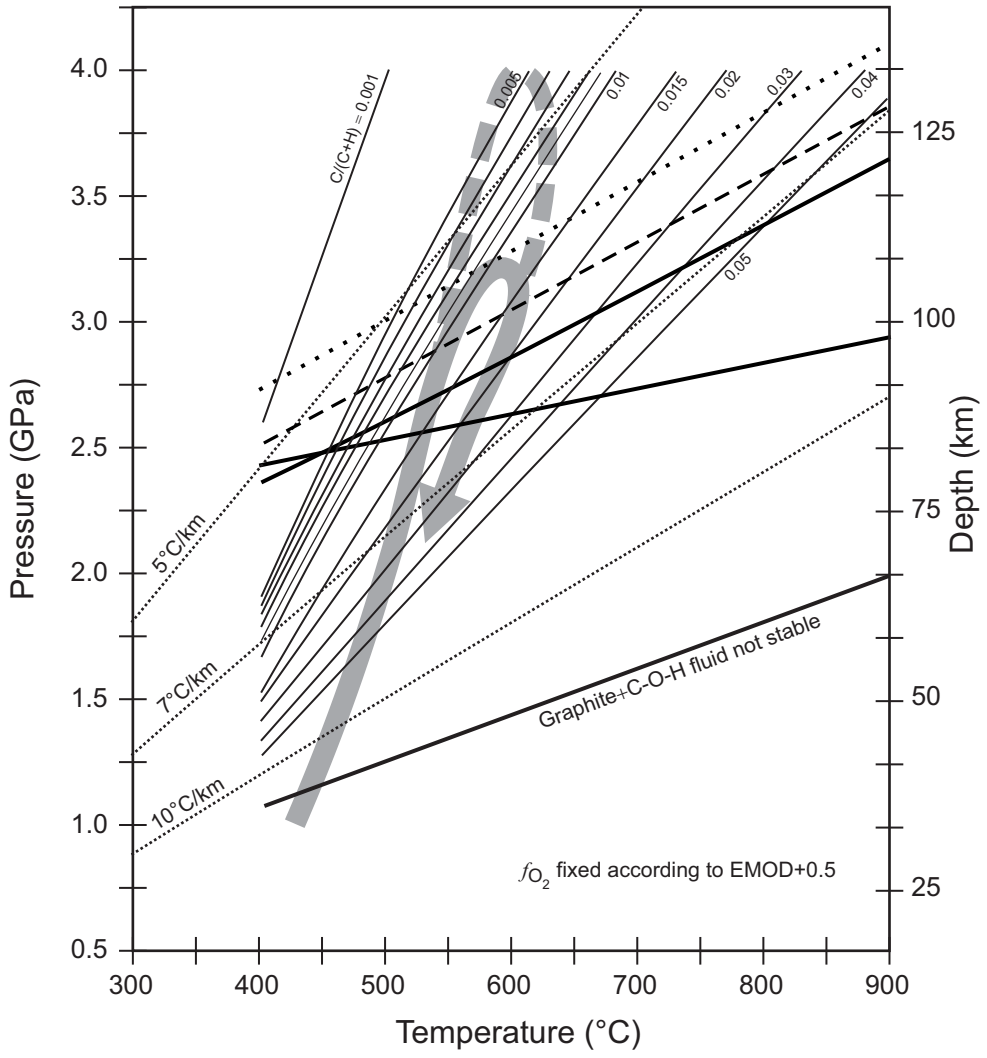
Pressure (GPa)
Depth (km)
Temperature (°C)
4.0
3.5
3.0
2.5
2.0
1.5
1.0
0.5
125
100
75
50
25
300
400
500
600
700
800
900
C/(C+H) = 0.001
0.005
0.01
0.015
0.02
0.03
0.04
0.05
5°C/km
7°C/km
10°C/km
Graphite+C-O-H fluid not stable
f_{O_2} fixed according to EMOD+0.5

Fig. 9

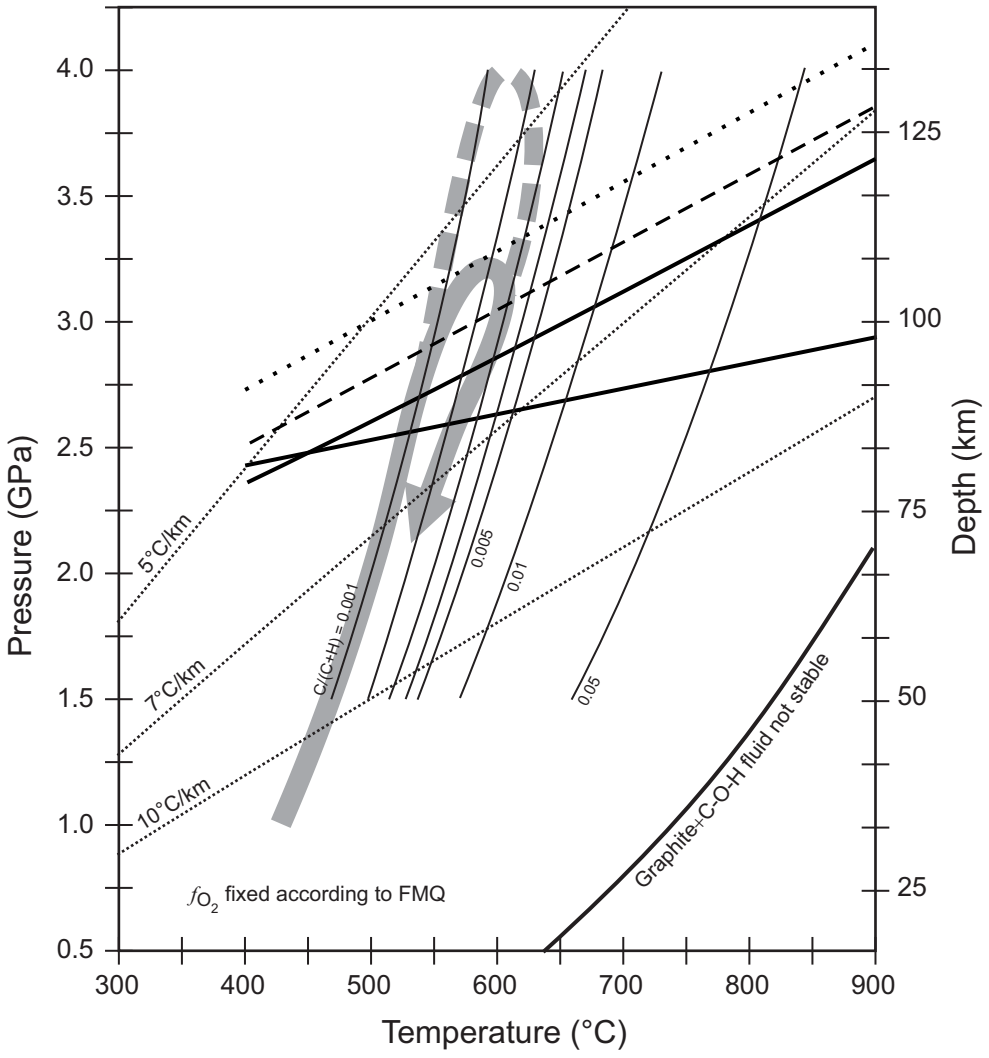
Pressure (GPa)
Depth (km)
Temperature (°C)
4.0
3.5
3.0
2.5
2.0
1.5
1.0
0.5
125
100
75
50
25
300
400
500
600
700
800
900
5°C/km
7°C/km
10°C/km
C/(C+H) = 0.001
0.005
0.01
0.05
Graphite+C-O-H fluid not stable
f_{O_2} fixed according to FMQ

Fig. 10